

Homogenization of rod-like metamaterials as a special Cosserat rod

Vinayak^a, Ajeet Kumar^a

^a*Department of Applied Mechanics, Indian Institute of Technology Delhi, New Delhi, India*

Abstract

Rod-like metamaterials are the structures that are obtained by periodically assembling its microstructural unit (network of rods) in just one direction. In this work, we present a scheme for obtaining the nonlinear constitutive response of such structures when homogenized macroscopically as a continuum rod. To capture accurately arbitrary and large deformation, the geometrically exact special Cosserat rod theory is used for modeling the rod at both micro and macro scales. By assuming the metamaterial structure to be strained uniformly (at macroscale) along its arc length, the full structure problem is reduced to just that of its microstructural unit but subjected to helically periodic boundary condition. The microscale problem, consisting of a network of rods and formulated in a variational setting, is solved in the presence of rod joint constraints and helically periodic boundary conditions. The expressions for the macroscale/homogenized rod's stress resultants (internal contact force and moment) and stiffnesses are then obtained. Finally, several numerical examples having different microstructural units/RVEs are presented to demonstrate our method. We start with simpler square and cross RVEs to validate our results with the existing literature. We then take up more complex RVEs such as square RVEs having helical constituent rods which have application as artificial muscle material and eventually we work on the homogenization of auxetic tubular metamaterials. We show how various design parameters of these RVEs can be tuned to obtain the desired macroscopic response.

Keywords: metamaterials; geometrically exact rods; multiscale modeling

1. Introduction

In pursuit of exotic material behavior, several man-made metamaterials have been proposed and developed. They have not only pushed the boundaries of stiffness and strength but have also opened the possibilities of tailored mechanical properties, e.g., negative Poisson's ratio, negative compressibility etc. (Jiao et al., 2023). Moreover, material properties beyond just mechanical such as thermal, electrical, electromechanical etc. are being envisioned (Jiao, 2023) that can be tuned as desired by tailoring their underlying microstructure. The advancement of additive manufacturing techniques has accelerated the development of such tailored microstructures resulting in the realization of exotic material properties. Predicting these properties beforehand forms an important cog in the design process of metamaterials. As conducting large scale experiments on such structures is not only difficult but also expensive, researchers have resorted to simulation driven design (Weeger et al., 2019). Metamaterials are essentially heterogeneous. Direct full-scale numerical simulation of such heterogeneous structures is computationally expensive. One can make use of homogenization techniques in case of periodic metamaterials wherein the heterogeneous metamaterial is replaced by a homogeneous continuum. The periodically

repeating microstructural unit is usually termed the representative volume element (RVE). Depending on the desired behaviour, an RVE can be constructed using network of rods (Fleck et al., 2010), plates (Lee et al., 2016) or three-dimensional solids (Krishnan et al., 2022). Rod-network based RVEs or lattices have conventionally been used for developing lightweight materials having high stiffnesses. However, their usage for high compliance applications such as for artificial tissues or as energy absorbing materials for high velocity impact applications (Chang et al., 2022; Surjadi and Portela, 2025) are being explored recently. In this work, we focus on metamaterials formed by periodically repeating such microstructural units in just one direction such that, macroscopically, the whole structure is much longer in one direction than the other two. We call such metamaterials rod-like metamaterials. They have found application as cardiovascular stents (Han and Lu, 2018), artificial muscles (Sun et al., 2025), robotic actuators (Parra Rubio et al., 2023), metamaterial shafts (Wu et al., 2025) etc. Furthermore, hierarchical metamaterials (Meza et al., 2015; Moestopo et al., 2020; Emami and Gross, 2024) have been proposed which can be thought of as a network of rod-like metamaterials. In this work, we propose a scheme for the homogenization of such rod-like metamaterials as a special Cosserat rod.

Homogenization techniques require separation of micro and macro length scales (Saeb et al., 2016). For three-dimensional metamaterials, this length-scale separation should hold in all three periodically repeating directions. To this end, analytical (Deshpande et al., 2001), asymptotic and computational models (Vigliotti and Pasini, 2012a,b) have been developed wherein a first-order homogenization technique has been used for small deformation of three-dimensional rod lattices. Herrnböck and Steinmann (2022) extended the computational homogenization for three-dimensional rod-lattices assuming finite strain at macroscale and geometrically exact elastoplastic beam elements at microscale. In case, the deformation at macroscale varies rapidly in space, first-order homogenization schemes become insufficient and one needs to resort to higher-order asymptotic (Rahali et al., 2015) and computational homogenization schemes (Geers et al., 2007; Glaesener et al., 2019; Weeger, 2021). More recently, Seppecher et al. (2011) and Audoly and Lestringant (2023) have used asymptotic techniques for the homogenization of linear elastic truss/beam lattices repeating periodically in arbitrary dimensions. Rod-like metamaterials which repeat in only one direction typically undergo deformations such as bending and twisting which involve significant level of strain gradient in cross-sectional plane. Therefore, first-order homogenization schemes for such deformations are insufficient. Another factor influencing the homogenization of rod-like metamaterials is that since it is periodic in only one direction, separation of length scale does not hold in other two directions and using three-dimensional homogenization schemes lead to size-effects (Yang and Müller, 2021; Alavi et al., 2022; Sarhil et al., 2023). Three-dimensional continua which are much larger in one direction than the other two are often modeled using Cosserat rod theory (Antman, 2005). This is not only computationally efficient, it also leads to convenient representation of deformations typical of such structures such as bending and twisting. However, one needs to know the effective constitutive behaviour of such continua when modeled as a rod.

In order to obtain constitutive response of continuum rods, both asymptotic (Yu et al., 2012; Audoly and Lestringant, 2021) and computational (Simo and Vu-Quoc, 1991; Chadha and Todd, 2019; Arora et al., 2019) homogenization models have been developed. These models are typically based on the assumption that the rod's strain parameters vary slowly

along the arc-length of the rod thus reducing the full rod problem to just a cross-section. The cases of bending and twisting involving large three-dimensional strain gradients in the cross-sectional plane are very well covered under such assumptions. Pertaining to the homogenization of rod-like metamaterials involving rod-network as their microstructural unit, interest in space applications has driven the development of analytical models (Noor et al., 1978; Renton, 1984; Burgardt and Cartraud, 1999; Kahla, 1995) that homogenized pin-jointed rod-like truss frames into continuum rods undergoing small deformations. More recent efforts have incorporated geometric nonlinearity at macroscale (Cao et al., 2020) and flexible joints at microscale (Liu et al., 2019). Likewise, Abdoul-Anziz and Seppecher (2018) and Audoly and Lestringant (2023) developed asymptotic models for the homogenization of linear elastic beam networks with arbitrary geometry and periodicity, recovering the Euler-Bernoulli and Timoshenko beam models as the homogenized continua in cases of one-dimensional periodicity. Ménard and Cartraud (2021) presented homogenization model for spiral-strand cables wherein the macroscale beam was considered to be a three-dimensional Euler-Bernoulli beam. Recently, Saadat and Durville (2023) proposed a novel computational homogenization model for spiral strands using geometrically exact rod model at both macro and micro scales. Neglecting shear deformation at macroscale, they employed a linear macro-to-micro transition which, we note, is applicable only when the rod’s strains are small enough. To homogenize discrete nanostructures such as carbon nanotubes as an effective Cosserat rod, Kumar et al. (2016) introduced the *helical Cauchy-Born (HCB) rule*. This approach leverages the helical periodicity of uniformly deformed slender structures to reduce the full structural problem to just its RVE. Their reduction also leads to a fully non-linear macro-to-micro transition for one-dimensional structures. The HCB model is geometrically exact at macroscale and also supports general constitutive behavior at microscale. It has since been extended to model nonlinear constitutive responses of anisotropic elasto-plastic rods (Vinayak et al., 2023), strips (Kumar et al., 2024) etc. In this work, we further extend the HCB model and propose a computational scheme to obtain the effective behavior of rod-like metamaterials wherein both the microscale rods and the macroscopic effective rod are modeled as special Cosserat rods. The proposed scheme uses fully nonlinear geometrically exact kinematics not just for the individual rod models at macro and micro scales but also for macro-to-micro transition: the macro-to-micro transition in Saadat and Durville (2023) isn’t geometrically exact and holds only for small enough values of macroscopic rod’s strain parameters. Furthermore, we assume arbitrary constitutive behavior of constituent rods in the metamaterial’s microstructural unit. Unlike the original HCB rule for nanorods (Kumar et al., 2016) where the energy at microscale (inter-atomic energy) was dependent only on the positions of atoms, the microscale energy in the present work depends on both positions and orientation of directors at every nodal points of microscale rods in the metamaterial’s RVE. In summary, the following are the novel contributions of this work:

1. Both microscale and macroscale rods are modeled as geometrically exact special Cosserat rods accounting for not just finite bending and twisting but also finite shear and stretch at both the scales.
2. A geometrically exact nonlinear map is proposed for applying helically periodic boundary condition to both translational and rotational degrees of freedom at microscale. The map holds even at large strains of macroscale rod.
3. The microscale rod’s constitutive model can be arbitrary.

The outline of the paper is as follows. In section 2, we briefly describe the geometrically exact special Cosserat rod theory. In Section 3, we obtain the formula for uniformly straining (at macroscale) a rod-like metamaterial along its arclength. In particular, we derive how do microscale rod's centerline and directors in the metamaterial's RVE relate to the corresponding variables in the images of the RVE. This leads to what we call helically periodic boundary condition. Section 4 derives various constraints such as joint constraints, helical boundary condition constraints and global constraints in the presence of which the RVE's energy needs to be minimized for homogenization. The constrained RVE energy functional and its weak form is presented in Section 5. In Section 6, we derive expressions of the homogenized rod's internal contact force, moment and stiffnesses at arbitrary state of macroscale rod's strain. In Section 7, we present a procedure to discretize the rod's energy using what we call helical elements. In Section 8, we present numerical examples involving different RVEs to demonstrate our scheme. First, we apply the proposed scheme to square- and cross-RVE based metamaterials. Then, we take up more complex square RVEs formed by helical rods and auxetic RVEs. Section 9 concludes our paper.

Notation: The following notations are used unless specified otherwise. Vectors are denoted by lowercase bold letters whereas second-order tensors are denoted by uppercase bold letters. The symbol $(\cdot)'$ represents derivative with respect to the rod's undeformed arc-length. Finally, repeated Latin indices imply summation from 1 to 3 whereas repeated Greek indices imply summation from 1 to 2.

2. Brief description of the geometrically exact rod theory

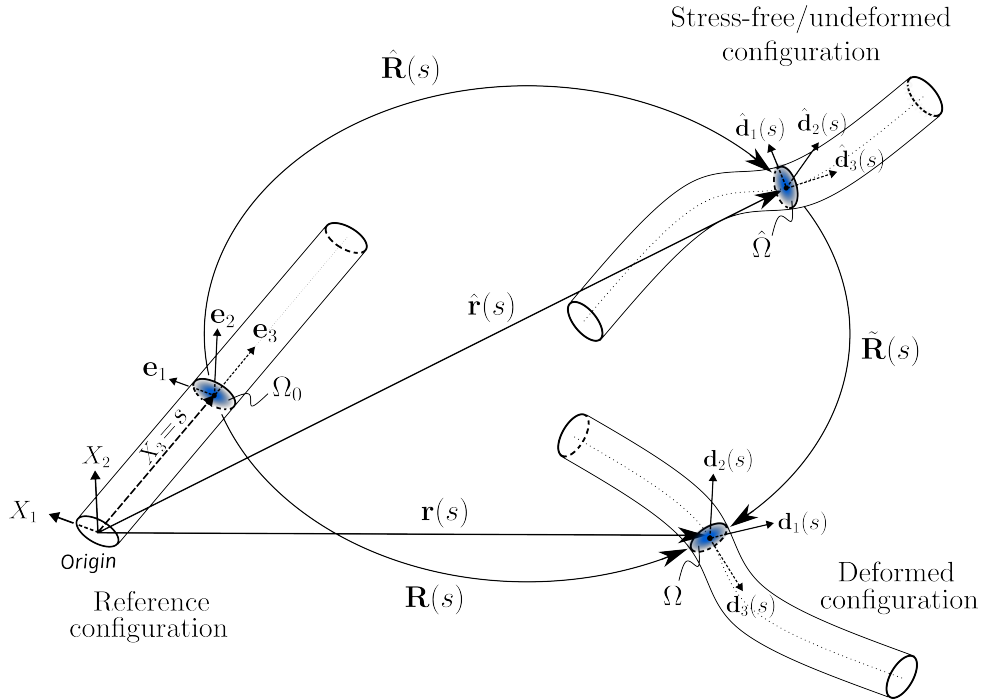


Figure 1: Kinematics of a special Cosserat rod

A continuum rod can be described as a set of infinite cross-sections stacked together along a curve, known as the centreline of the rod. The orientation of the cross-section is given by a triad of orthonormal directors as shown in Figure 1. The reference centerline of

the rod is represented by the straight line $s\mathbf{e}_3$ where $s \in [0, l]$ and the orthonormal director triads coincide with the global basis in the reference state. In the stress-free configuration, the centreline is given by $\hat{\mathbf{r}}(s)$ whereas the director triads are given by $(\hat{\mathbf{d}}_1(s), \hat{\mathbf{d}}_2(s), \hat{\mathbf{d}}_3(s))$. The associated rotation tensor in the stress-free configuration is $\hat{\mathbf{R}}(s)$ such that

$$\hat{\mathbf{d}}_i(s) = \hat{\mathbf{R}}(s)\mathbf{e}_i. \quad (1)$$

Finally, the deformed configuration is given by the centreline curve $\mathbf{r}(s)$ and the director triads $(\mathbf{d}_1(s), \mathbf{d}_2(s), \mathbf{d}_3(s))$ such that

$$\mathbf{d}_i(s) = \mathbf{R}(s)\mathbf{e}_i. \quad (2)$$

In this work, we parameterize the rotation tensor using a vector $\boldsymbol{\theta} \in \mathbb{R}^3$ whose direction coincides with the axis of rotation and whose magnitude equals the angle of rotation. The rotation tensor $\mathbf{R}(\boldsymbol{\theta}(s))$ is then obtained using the Rodrigue's rotation formula (refer to equation (A.1)). Therefore, the variables $\mathbf{r}(s)$ and $\boldsymbol{\theta}(s)$ become the kinematic variables of this theory. The strain measures in this theory are

$$\mathbf{v}_0 = \mathbf{R}^T \mathbf{r}' = v_i \mathbf{e}_i, \quad (3)$$

$$\mathbf{k}_0 = \text{axial}(\mathbf{K}_0) = \kappa_i \mathbf{e}_i \text{ where } \mathbf{K}_0 = \mathbf{R}^T \mathbf{R}'. \quad (4)$$

Here (v_1, v_2) are the shear strains, v_3 is the axial stretch, (κ_1, κ_2) are the bending curvatures and κ_3 is the twist. The spatial counterparts of the above strain measures are

$$\mathbf{v} = \mathbf{R}\mathbf{v}_0 = \mathbf{r}' = v_i \mathbf{d}_i, \quad (5)$$

$$\mathbf{k} = \text{axial}(\mathbf{K}) = \kappa_i \mathbf{d}_i \text{ where } \mathbf{K} = \mathbf{R}\mathbf{K}_0\mathbf{R}^T = \mathbf{R}'\mathbf{R}^T. \quad (6)$$

The internal contact force $\mathbf{n}(s)$ and internal contact moment $\mathbf{m}(s)$ acting on a cross-section of the rod in the current configuration are given by

$$\mathbf{n} = n_i \mathbf{d}_i, \quad \mathbf{m} = m_i \mathbf{d}_i \quad (7)$$

while its rotational pull-backs are given by

$$\mathbf{n}_0 = n_i \mathbf{e}_i, \quad \mathbf{m}_0 = m_i \mathbf{e}_i, \quad (8)$$

respectively. Together, they are also called the rod's stress resultants. The linear and angular momentum balance equations of the rod assuming statics condition are given by

$$\begin{aligned} \mathbf{n}' + \hat{\mathbf{n}} &= \mathbf{0}, \\ \mathbf{m}' + \mathbf{v} \times \mathbf{n} + \hat{\mathbf{m}} &= \mathbf{0}. \end{aligned} \quad (9)$$

Here $\hat{\mathbf{n}}$ and $\hat{\mathbf{m}}$ are the distributed force and couple, respectively, that act on the rod. One further assumes the existence of a scalar-valued function $\phi(\mathbf{v}_0, \mathbf{k}_0)$ denoting stored energy per unit undeformed length such that

$$\mathbf{n}_0 = \frac{\partial \phi}{\partial \mathbf{v}_0}, \quad \mathbf{m}_0 = \frac{\partial \phi}{\partial \mathbf{k}_0}, \quad \mathbb{C}_0^{rod} = \frac{\partial^2 \phi}{\partial[\mathbf{v}_0, \mathbf{k}_0] \partial[\mathbf{v}_0, \mathbf{k}_0]}. \quad (10)$$

Here \mathbb{C}_0^{rod} is the rod's elasticity tensor whose diagonal components are the shearing,

stretching, bending and twisting stiffnesses whereas the off-diagonal components are the various coupling stiffnesses. It assumes a diagonal form for isotropic rods. Often, the following quadratic energy model is assumed with \mathbb{C}_0^{rod} being a constant tensor:

$$\phi(\mathbf{v}_0, \mathbf{k}_0) = \frac{1}{2} \begin{bmatrix} \mathbf{v}_0 - \hat{\mathbf{v}}_0 \\ \mathbf{k}_0 - \hat{\mathbf{k}}_0 \end{bmatrix}^T \mathbb{C}_0^{rod} \begin{bmatrix} \mathbf{v}_0 - \hat{\mathbf{v}}_0 \\ \mathbf{k}_0 - \hat{\mathbf{k}}_0 \end{bmatrix}. \quad (11)$$

Here $\hat{\mathbf{v}}_0$ and $\hat{\mathbf{k}}_0$ are the strain measures in the rod's stress-free/natural configuration. The quadratic model works for small departure of strain values from their values in the natural state. For large enough departure from natural strain values, a nonlinear energy model would be required that should include the effect of the underlying nonlinear three-dimensional material behavior of the rod material as well as nonlinear cross-sectional warping. Arora et al. (2019) proposed a ‘‘cross-sectional warping problem’’ to obtain this nonlinear energy numerically. They employ helical Cauchy-Born rule to subject the rod to a strain field which is uniform in the rod's arclength - this reduces the equations of elasticity from the entire rod body to just its cross-section. The rod's energy is then obtained by integrating the three-dimensional stored energy density W in the rod's cross-section as follows:

$$\phi(\mathbf{v}_0, \mathbf{k}_0) = \int_{\Omega_0} W(\mathbf{F}(\mathbf{v}_0, \mathbf{k}_0)) dX_1 dX_2. \quad (12)$$

Here \mathbf{F} is the three-dimensional deformation gradient tensor which is obtained through the map

$$\mathbf{x}(X_1, X_2, s) = \mathbf{r}(s) + \mathbf{R}(s)\mathbf{x}_w(X_1, X_2) \quad (13)$$

where

$$\mathbf{x}_w(X_1, X_2) = X_\alpha \mathbf{e}_\alpha + u_i(X_1, X_2) \mathbf{e}_i \quad (14)$$

is the warped cross-section's map and u_i denote the unknown in-plane and out-of-plane warping displacement components which are obtained by solving the above mentioned cross-sectional warping problem. In this work, we use a similar approach to obtain ϕ for a rod-like metamaterial. As we show next, instead of solving the cross-sectional warping problem, one has to solve the metamaterial RVE's ‘‘warping problem’’.

3. Rod-like metamaterials strained uniformly (at macroscale) along its arclength

We will treat rod-like metamaterials as a homogenized continuum rod at macroscale and the metamaterial's RVE as the microstructure of this homogenized rod. In order to obtain ϕ for such rod-like metamaterials, we think of macroscopically subjecting it to a strain field which is uniform in its arc-length at macroscale, i.e., $\mathbf{v}_0(s^M) = \mathbf{v}_0^M$ and $\mathbf{k}_0(s^M) = \mathbf{k}_0^M$. Here s^M denotes the macroscale arc-length parameter. The macroscopic configuration $(\mathbf{r}^M, \mathbf{R}^M)$ of such a homogenized rod is obtained by integrating (3) and (4) which results

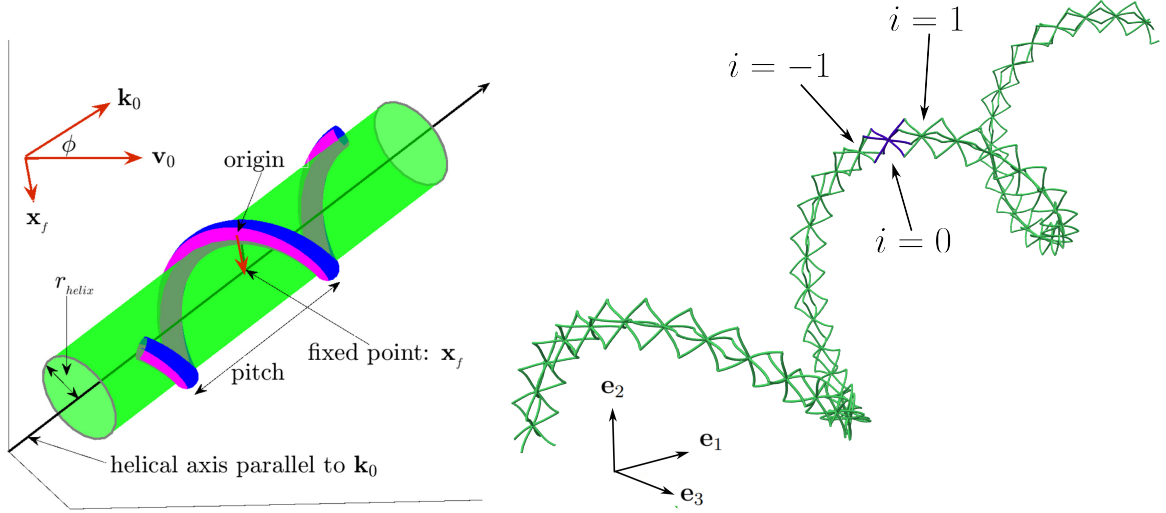


Figure 2: Uniformly strained continuum rod (left)(Kumar et al., 2016) and rod-like metamaterial (right).

in a uniform helical rod given by¹ (also see Figure 2a):

$$\mathbf{r}^M(s^M) = \left(\int_0^{s^M} \mathbf{R}^M(l) dl \right) \mathbf{v}_0^M, \quad \mathbf{R}^M(s^M) = e^{s^M \mathbf{K}_0^M}. \quad (15)$$

Substituting (15) in (13) and further generalizing it for rod-like metamaterials, we get

$$\mathbf{x}^i(X_1^m, X_2^m, s^m) = \left(\int_0^{iL} \mathbf{R}^M(l) dl \right) \mathbf{v}_0^M + \mathbf{R}^M(iL) \mathbf{x}^{RVE}(X_1^m, X_2^m, s^m) \quad (16)$$

where \mathbf{x}^i is the i^{th} image of the metamaterial's RVE (corresponding to $i = 0$ in Figure 2b) whose deformed position is denoted by \mathbf{x}^{RVE} in the above equation. The macroscale arc-length parameter s^M is replaced here by iL where L is the extent of the RVE along the axis of the homogenized rod in its reference state. Likewise, (X_1^m, X_2^m, s^m) denote the referential microscopic coordinates of material points in the RVE. Note that $s^m \neq s^M$: the variable s^m typically runs within an RVE. Also note that the role of the unknown warped cross-section \mathbf{x}_w in (13) is overtaken by the unknown warped/deformed RVE, i.e., \mathbf{x}^{RVE} in equation (16). In case, the RVE comprises of a network of rods (as in Figure 2b) which is the focus in this work, the unknowns in the RVE would simply be the centerline and rotation of all the rods in the RVE, i.e., $\{\mathbf{r}^\alpha(s^\alpha), \mathbf{R}^\alpha(s^\alpha)\}_{\alpha=1}^{N_{rods}}$ where s^α denotes the arc-length parameter for the α^{th} rod in the RVE and N_{rods} is the total number of rods in the RVE. For example, the rod-like metamaterial in Figure 4 has six rods (all shown in black) in its RVE - the green vertical rod at the right boundary is not a part of the RVE but its right image. Equation (16) then gets modified as follows:

$$\begin{aligned} \mathbf{r}^{i,\alpha}(s^\alpha) &= \left(\int_0^{iL} \mathbf{R}^M(l) dl \right) \mathbf{v}_0^M + \mathbf{R}^M(iL) \mathbf{r}^\alpha(s^\alpha), \\ \mathbf{R}^{i,\alpha}(s^\alpha) &= \mathbf{R}^M(iL) \mathbf{R}^\alpha(s^\alpha). \end{aligned} \quad (17)$$

¹The superscript M here denotes that they are macroscopic variables.

Here $(\mathbf{r}^{i,\alpha}(s^\alpha), \mathbf{R}^{i,\alpha}(s^\alpha))$ denotes the centerline and rotation tensor of the α^{th} rod in the i^{th} image of the RVE. In the subsequent section, we propose the RVE problem to determine the unknowns $\{\mathbf{r}^\alpha, \mathbf{R}^\alpha\}_{\alpha=1}^{N_{rods}}$. We also use the following notation for the position of different nodes of a rod in the RVE:

$$\mathbf{r}_k^\alpha = \mathbf{r}^\alpha(s_k^\alpha) \quad \text{for the } k^{th} \text{ internal node located at } s_k \in (0, L^\alpha). \quad (18)$$

For the rod's two end-points in particular, we use the following notation:

$$\mathbf{r}_\beta^\alpha = \begin{cases} \mathbf{r}_+^\alpha & \text{for } \mathbf{r}^\alpha(L^\alpha) \\ \mathbf{r}_-^\alpha & \text{for } \mathbf{r}^\alpha(0) \end{cases} \quad (19)$$

3.1. Metamaterial RVE's "warping problem"

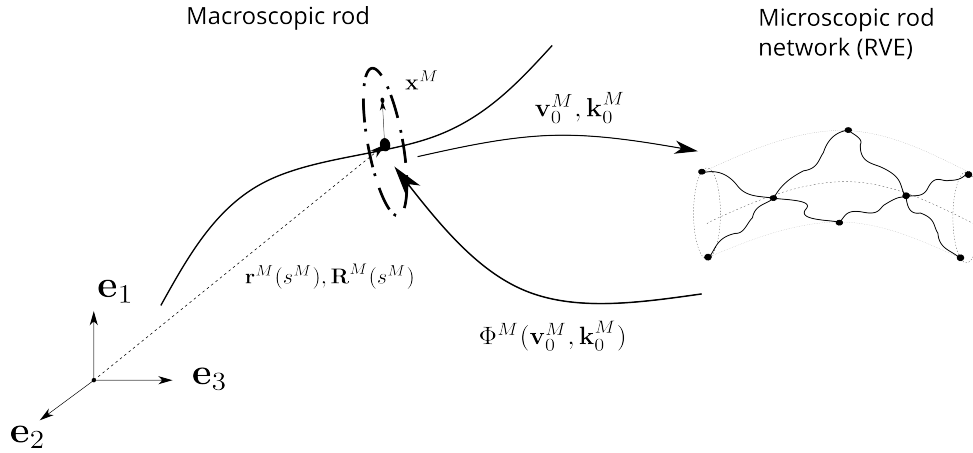


Figure 3: Multiscale framework for rod-like metamaterials

Figure 3 shows the centerline of a long homogenized macroscopic rod whose "cross-section" is formed by the metamaterial's RVE.² The macroscopic rod is typically subjected to a non-uniform strain field $(\mathbf{v}_0^M(s^M), \mathbf{k}_0^M(s^M))$. If this strain field varies slowly along the arc-length, one can think of the strain field as being "locally uniform". One can then construct a fictitious macroscopic rod or metamaterial that is uniformly strained with the actual rod's local value of strain $(\mathbf{v}_0^M, \mathbf{k}_0^M)$ - the fictitious metamaterial will deform helically obeying equation (17). In this section, we use this helical symmetry to formulate the microscale RVE warping problem to obtain the energy density Φ^M of the actual rod-like metamaterial (modeled as a homogenized macroscale rod) as follows:

$$\Phi^M(\mathbf{v}_0^M, \mathbf{k}_0^M) = \frac{1}{L} \min_{\{\mathbf{r}^\alpha, \mathbf{R}^\alpha\}} \mathcal{E}^{RVE} = \frac{1}{L} \min_{\{\mathbf{r}^\alpha, \mathbf{R}^\alpha\}} \left(\sum_{\alpha=1}^{N_{rods}} \int_0^{L^\alpha} \phi^\alpha(\mathbf{v}_0^\alpha, \mathbf{k}_0^\alpha) ds^\alpha \right) \quad (20)$$

where \mathcal{E}^{RVE} is the elastic energy stored in the RVE of the fictitious uniformly deformed metamaterial. The microscopic rods within the RVE are also modeled as being geomet-

²A rod's cross-section has zero thickness in continuum sense. However, the metamaterial's RVE has finite extent along the rod's arclength. As the length of the RVE is typically much smaller compared to the metamaterial's total length (only then the separation of length scale holds), we can therefore call the RVE here to be the metamaterial's "cross-section".

rically exact as mentioned earlier. The minimization problem (20) needs to be solved in the presence of following three constraints: (i) internal joint constraints - to enforce connectivity of rods within the RVE (ii) helical boundary condition constraint - to apply helical periodicity and (iii) global constraints - to restrict rigid translation and rotation of the RVE as a whole and also to keep the macroscopic strain parameters fixed during minimization. A pictorial illustration of these constraints is shown in Figure 4. We discuss

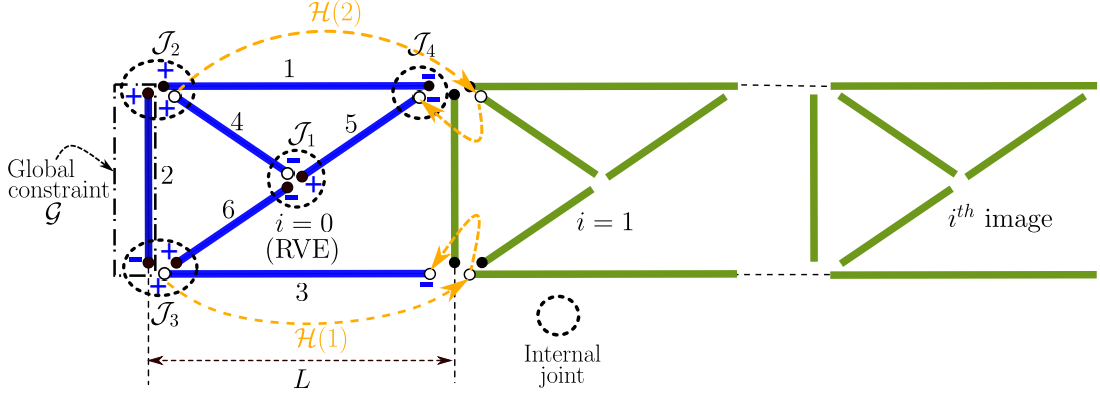


Figure 4: Various constraints needed for the homogenization of rod-like metamaterials

these constraints in detail next.

4. Constraints in the RVE problem

4.1. Internal joints in the RVE

We assume that the RVE is a network of rods consisting of N_J internal joints. By *internal*, we imply that all the rods participating in a joint are internal to the RVE. Let us assume the connection between the rods to be rigid and use the master-slave approach to formulate the internal joint constraints (Jelenić and Crisfield, 1996; Ibrahimbegović and Mamouri, 2000).³ For the i^{th} joint in the RVE, we assume it to be formed by J_i number of nodes each belonging to different rods that join there and denote this set of nodes by \mathcal{J}_i . It is defined as follows:

$$\mathcal{J}_i = \{(\alpha, \beta) : \mathbf{r}_\beta^\alpha \text{ lies at the } i^{\text{th}} \text{ joint}\}, |\mathcal{J}_i| = J_i \quad \forall i = 1 : N_J \quad (21)$$

Here β takes either '+' or '-' value. Each set \mathcal{J}_i is an ordered set such that its first element $\mathcal{J}_i(1) = (\alpha_1, \beta_1)$ is the master node and all the other elements $\mathcal{J}_i(k) = (\alpha_k, \beta_k)$ where $k \in [2, J_i]$ are slave nodes. In the RVE of Figure 4, there are four internal joints whose sets are given by

$$\begin{aligned} \mathcal{J}_1 &= \{(4, -), (6, -), (5, +)\}, \\ \mathcal{J}_2 &= \{(4, +), (2, +), (1, +)\}, \\ \mathcal{J}_3 &= \{(3, +), (2, -), (6, +)\}, \\ \mathcal{J}_4 &= \{(5, -), (1, -)\}. \end{aligned} \quad (22)$$

³Other kinds of joints such as pinned joint or ball-and-socket joint can also be easily incorporated.

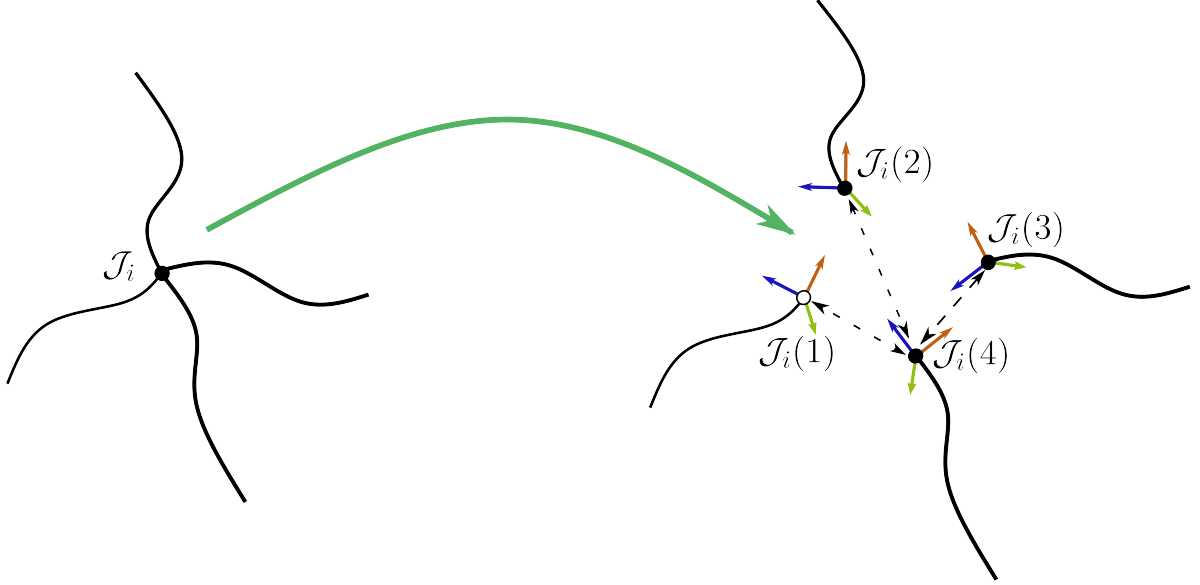


Figure 5: A schematic of multiple rods connections at a joint. Here, the joint \mathcal{J}_i contains $J_i = 4$ nodes. The master node given by $\mathcal{J}_i(1)$ is shown as a white circle. All the other nodes, shown as black circles, are slaves to the master node in this joint.

Once internal joints are defined, for an i^{th} joint, we have the following translational constraint relating the positions of master and slave nodes:

$$\mathcal{J}_{i,k}^{trans} \equiv \mathbf{r}_{\beta_1}^{\alpha_1} - \mathbf{r}_{\beta_k}^{\alpha_k} = \mathbf{0} \quad \forall k \in [2, J_i] \text{ where } (\alpha_k, \beta_k) = \mathcal{J}_i(k). \quad (23)$$

Likewise, the relative angle between the directors of master and slave nodes is constrained as follows:

$$\mathbf{d}_{\beta_1,p}^{\alpha_1} \cdot \mathbf{d}_{\beta_k,q}^{\alpha_k} = \hat{\mathbf{d}}_{\beta_1,p}^{\alpha_1} \cdot \hat{\mathbf{d}}_{\beta_k,q}^{\alpha_k} \quad \forall k \in [2, J_i] \text{ and } p, q \in 1, 2, 3. \quad (24)$$

Here $\mathbf{d}_{\beta_k,q}^{\alpha_k}$ refers to the q^{th} director of k^{th} node at i^{th} internal joint in the RVE. The above equation leads to

$$(\mathbf{R}_{\beta_k}^{\alpha_k})^T \mathbf{R}_{\beta_1}^{\alpha_1} = (\hat{\mathbf{R}}_{\beta_k}^{\alpha_k})^T \hat{\mathbf{R}}_{\beta_1}^{\alpha_1} \quad (25)$$

implying that the relative three-dimensional rotation tensor between the director frames of the master node and all slave nodes is preserved during deformation. This will also automatically ensure that the relative rotation between director frames of every pair of slave nodes is also preserved. Thus, the internal joint rotational constraint at i^{th} joint is given by

$$\mathcal{J}_{i,k}^{rot} \equiv axial \left(\log \left(\left((\mathbf{R}_{\beta_k}^{\alpha_k})^T \mathbf{R}_{\beta_1}^{\alpha_1} \right) \left((\hat{\mathbf{R}}_{\beta_k}^{\alpha_k})^T \hat{\mathbf{R}}_{\beta_1}^{\alpha_1} \right)^T \right) \right) = \mathbf{0} \quad \forall k \in [2, J_i]. \quad (26)$$

Here the *axial* function returns axial vector of the skew-symmetric tensor.

4.2. Helical boundary condition

The idea here is to express the position and directors associated with the nodes located at the RVE's right boundary in terms of their corresponding values from the RVE's left boundary. This enforces what we call *helical boundary condition*. Let us construct a

set \mathcal{H} of all such nodes at the right boundary and their counterpart nodes at the left boundary.⁴ This set is also assumed to be ordered so that all left nodes appear first followed by all right nodes. Furthermore, for k^{th} left node in the set, i.e., $\mathcal{H}(k) = (\alpha_k, \beta_k)$, its corresponding right node is $\mathcal{H}(k + N_H) = (\alpha_{k_r}, \beta_{k_r})$ for all $k \in \{1, 2, 3, \dots, N_H\}$ and $k_r = k + N_H$. Here N_H is the total number of such nodes at the right boundary. For the RVE in Figure 4, $N_H = 2$ and the helical set \mathcal{H} is given by

$$\mathcal{H} = \{(3, +), (4, +), (3, -), (5, -)\}. \quad (27)$$

As mentioned earlier, since joint \mathcal{J}_4 lies at the right boundary, only its master node, i.e., (5,-) is considered in the helical set. We now obtain the mathematical relations which enforce *helical boundary condition*. Using HCB rule (17) on the left boundary nodes from the set \mathcal{H} , we have

$$\mathbf{r}_{\beta_k}^{1, \alpha_k} = \left(\int_0^L \mathbf{R}^M(l) dl \right) \mathbf{v}_0^M + \mathbf{R}(L) \mathbf{r}_{\beta_k}^{\alpha_k} \quad \forall k \in [1, N_H] \text{ such that } (\alpha_k, \beta_k) = \mathcal{H}(k). \quad (28)$$

Now, since the right boundary nodes of the RVE form rigid joint with the left boundary nodes of the image RVE corresponding to $i = 1$, we get

$$\mathbf{r}_{\beta_{k_r}}^{\alpha_{k_r}} = \mathbf{r}_{\beta_k}^{1, \alpha_k}. \quad (29)$$

Using equations (28) and (29), we then get the following translational helical constraint relating the left and right boundary nodes in the helical set \mathcal{H} :

$$\mathcal{H}_k^{\text{trans}} := \mathbf{r}_{\beta_{k_r}}^{\alpha_{k_r}} - \left(\int_0^L \mathbf{R}^M(l) dl \right) \mathbf{v}_0^M - \mathbf{R}^M(L) \mathbf{r}_{\beta_k}^{\alpha_k} = \mathbf{0} \quad \forall k \in [1, N_H] \text{ and } k_r = k + N_H. \quad (30)$$

Likewise, the director triads of the left and right boundaries nodes in \mathcal{H} also need to be related. Essentially, the angle between the macroscopic directors at the RVE's left boundary and the microscopic directors of the RVE's left boundary nodes should be the same as the angle between the macroscopic directors at the left boundary of the image RVE and the microscopic directors of the image RVE's left boundary nodes, i.e.,

$$\mathbf{d}_p^M(0) \cdot \mathbf{d}_{\beta_{k,q}}^{\alpha_k} = \mathbf{d}_p^M(iL) \cdot \mathbf{d}_{\beta_{k,q}}^{i, \alpha_k} \quad \forall p, q \in 1, 2, 3 \quad (31)$$

where

$$\mathbf{d}_p^M(0) = \mathbf{R}^M(0) \mathbf{e}_p = \mathbf{e}_p, \quad \mathbf{d}_p^M(iL) = \mathbf{R}^M(iL) \mathbf{e}_p \quad (32)$$

are the director vectors associated with the macroscopic rod's cross-section. We have taken $\mathbf{R}^M(0) = \mathbf{I}$ here without any loss of generality. The above two equations then yield

$$\mathbf{R}_{\beta_k}^{i, \alpha_k} = \mathbf{R}^M(iL) \mathbf{R}_{\beta_k}^{\alpha_k}. \quad (33)$$

We have obtained a relation for rotation between the nodes lying on the left boundary of the RVE and the corresponding nodes lying in the i^{th} image of the RVE. Let us now use

⁴In case a joint lies at the right boundary, only the master node from the joint is taken in the set \mathcal{H} .

the joint constraint equation (25) to relate rotation between right boundary nodes of the RVE and the left boundary nodes of the image RVE, i.e,

$$\left(\mathbf{R}_{\beta_k}^{1,\alpha_k}\right)^T \mathbf{R}_{\beta_{k_r}}^{\alpha_{k_r}} = \left(\hat{\mathbf{R}}_{\beta_k}^{1,\alpha_k}\right)^T \hat{\mathbf{R}}_{\beta_{k_r}}^{\alpha_{k_r}} \quad \forall \quad k \in [1, N_H] \text{ and } k_r = k + N_H. \quad (34)$$

Let us further assume without loss of generality that the metamaterial or the macroscopic rod is straight and untwisted in its reference configuration, i.e, $\hat{\mathbf{R}}^M(iL) = \mathbf{I}$. Hence, using (33), we can write

$$\hat{\mathbf{R}}_{\beta_k}^{i,\alpha_k} = \hat{\mathbf{R}}_{\beta_k}^{\alpha_k}. \quad (35)$$

Substituting equations (33) and (35) into (34), we then obtain

$$\begin{aligned} \mathbf{R}_{\beta_{k_r}}^{\alpha_{k_r}} &= \mathbf{R}^M(L) \mathbf{R}_{\beta_k}^{\alpha_k} \left(\hat{\mathbf{R}}_{\beta_k}^{\alpha_k}\right)^T \hat{\mathbf{R}}_{\beta_{k_r}}^{\alpha_{k_r}} \\ \Rightarrow \mathbf{R}_{\beta_{k_r}}^{\alpha_{k_r}} \left(\hat{\mathbf{R}}_{\beta_{k_r}}^{\alpha_{k_r}}\right)^T &= \mathbf{R}^M(L) \mathbf{R}_{\beta_k}^{\alpha_k} \left(\hat{\mathbf{R}}_{\beta_k}^{\alpha_k}\right)^T. \end{aligned} \quad (36)$$

The above equation can be interpreted as follows: the relative rotation between current and reference states of microscopic right boundary directors differs from those of microscopic left boundary directors by macroscopic rotation $\mathbf{R}^M(L)$. The rotational helical boundary constraint then becomes

$$\mathcal{H}_k^{rot} \equiv axial \left(\log \left(\left(\mathbf{R}_{\beta_{k_r}}^{\alpha_{k_r}} \left(\hat{\mathbf{R}}_{\beta_{k_r}}^{\alpha_{k_r}}\right)^T \right) \left(\mathbf{R}^M(L) \mathbf{R}_{\beta_k}^{\alpha_k} \left(\hat{\mathbf{R}}_{\beta_k}^{\alpha_k}\right)^T \right)^T \right) \right) = 0. \quad (37)$$

Equations (30) and (37) together form the helical boundary condition constraints for the RVE problem. It is through these constraints that the cognizance of macroscopic rod's strain parameters $(\mathbf{v}_0, \mathbf{k}_0)$ is taken while solving the microscopic RVE problem. Hence, they can also be called the macro-to-micro transition maps in this theory. These maps are nonlinear, geometrically exact and hold even for large values of strain parameters $(\mathbf{v}_0, \mathbf{k}_0)$. In contrast, the macro-to-micro transition map proposed in Saadat and Durville (2023) holds only when the rod's strain parameters are small enough. Also note that here we have determined the helical boundary condition constraints purely based on kinematics - similar to the approach in Vigliotti and Pasini (2012b) for three-dimensional homogenization. This is in contrast with other approaches where Hill-Mandel condition is used to derive periodic boundary condition (Saeb et al., 2016; Weeger, 2021; Herrnböck and Steinmann, 2022).

4.3. Global constraints

In order to restrict rigid translation and rigid rotation of the RVE about the helical axis as well as to keep the imposed macroscopic strain parameters $(\mathbf{v}_0^M, \mathbf{k}_0^M)$ unchanged during energy minimization, we also need to apply certain global constraints (Kumar et al., 2016). Basically, one has to ensure that the centerline position of the macroscopic rod at $s^M = 0$ coincides with the origin and the rotation of the macroscopic rod's cross-section at $s^M = 0$ is identity in order to satisfy the macroscopic helical rod equation (15). Microscopically, at the RVE level, this is enforced by ensuring that the centroid of the material points on the left boundary of the RVE remains at origin and the left face of the RVE remains

oriented in $(\mathbf{e}_1 - \mathbf{e}_2)$ plane in an average sense.⁵ Let \mathcal{G} denote the set of all nodes lying on the left boundary of the RVE. In case, an internal joint lies on the left boundary, only the master node from the joint is considered in the set \mathcal{G} . It is also possible that a full rod lies on the left boundary in which case even the internal nodes of this rod would lie in the set \mathcal{G} . For the RVE in Figure 4, this set can be written as follows:

$$\mathcal{G} = \{(4, +), (3, +)\} + \text{all internal nodes of rod \#2} \quad (38)$$

The number of elements in this set will be denoted by N_G . In order to fix the center of all the nodes in \mathcal{G} to be at the origin, we have the following constraint:

$$\mathbf{g}^{trans} \equiv \sum_{\substack{k=1 \\ (\alpha_k, \beta_k) \in \mathcal{G}(k)}}^{N_G} \mathbf{r}_{\beta_k}^{\alpha_k} = \mathbf{0}. \quad (39)$$

To set the orientation of the left face of the RVE, we simply set all the three mixed moments of area corresponding to the nodes in \mathcal{G} to zero, i.e.,

$$\mathbf{g}^{rot} = \sum_{k=1}^{N_G} \mathbf{m}_{\beta_k}^{\alpha_k} = \mathbf{0} \quad (40)$$

where

$$\mathbf{m}_{\beta_k}^{\alpha_k} = r_{\beta_k,2}^{\alpha_k} r_{\beta_k,3}^{\alpha_k} \mathbf{e}_1 + r_{\beta_k,1}^{\alpha_k} r_{\beta_k,3}^{\alpha_k} \mathbf{e}_2 + r_{\beta_k,1}^{\alpha_k} r_{\beta_k,2}^{\alpha_k} \mathbf{e}_3. \quad (41)$$

Yeoh et al. (2022) imposed a similar constraint wherein the averaged moment of the microscopic and macroscopic displacements on the left boundary of a three dimensional continuum RVE are equalled. This was shown to restrict the rigid body rotation arising due to shear. We call the constraint in equation (40) as the “mmm” constraint. For RVEs with symmetric left face (such as in the case of a BCC lattice), one needs to modify the third constraint in (40) as follows:

$$\mathbf{m}_{\beta_k,3}^{\alpha_k} = \left[\arctan \left(\frac{r_{\beta_k,2}^{\alpha_k}}{r_{\beta_k,1}^{\alpha_k}} \right) - \arctan \left(\frac{R_{\beta_k,2}^{\alpha_k}}{R_{\beta_k,1}^{\alpha_k}} \right) \right]. \quad (42)$$

This new constraint is called “mmt” constraint which is more versatile but at the same time also more complex than “mmm” constraint. Note that we have used positional coordinates of nodes in \mathcal{G} to preserve orientation of the RVE. However, we also have directors associated with every node which represent microscopic rotations within the RVE. One could also think of tying the average of these micro-rotations with macroscopic orientation. This could be done by ensuring that the average change in rotation of the

⁵In our numerical experiments, we note that applying these global constraints on the left face alone is enough. If one also includes internal nodes of the RVE in these global constraints, the global constraint is found to be too restrictive leading to less accurate response.

directors of nodes in set \mathcal{G} must be zero, i.e.,

$$\mathbf{g}^{rot} = \sum_{k=1}^{N_G} \Delta \boldsymbol{\theta}_{\beta_k}^{\alpha_k} = \mathbf{0}. \quad (43)$$

Here the rotation vector $\Delta \boldsymbol{\theta}_{\beta_k}^{\alpha_k}$ is defined as follows:

$$\mathbf{R}(\boldsymbol{\theta}_{\beta_k}^{\alpha_k}) = \exp^{\Delta \boldsymbol{\theta}_{\beta_k}^{\alpha_k}} \mathbf{R}(\hat{\boldsymbol{\theta}}_{\beta_k}^{\alpha_k}). \quad (44)$$

We call this constraint as ‘‘delta-theta’’ constraint. One could also define $\Delta \boldsymbol{\theta}_{\beta_k}^{\alpha_k} = \boldsymbol{\theta}_{\beta_k}^{\alpha_k} - \hat{\boldsymbol{\theta}}_{\beta_k}^{\alpha_k}$ as in [Abdoul-Anziz and Seppcher \(2018\)](#) and [Ćanić et al. \(2022\)](#).⁶ These two definitions become the same for planar rotations as planar rotations are additive. In this work, we use the ‘‘delta-theta’’ type constraint given by (43). We now propose the RVE problem.

5. Constrained minimization of RVE energy

To solve the constrained minimization problem discussed above, we define the following constrained energy functional:

$$\mathcal{E}^{cons} = \mathcal{E}^{RVE} + \mathcal{C}^G + \mathcal{C}^H + \mathcal{C}^J \quad (45)$$

where the constraint terms are as follows:

$$\mathcal{C}^G = \begin{bmatrix} \boldsymbol{\lambda} \\ \boldsymbol{\mu} \end{bmatrix} \cdot \begin{bmatrix} \mathbf{g}^{trans} \\ \mathbf{g}^{rot} \end{bmatrix}, \quad \mathcal{C}^H = \sum_{k=1}^{N_H} \begin{bmatrix} \mathbf{h}_k^n \\ \mathbf{h}_k^m \end{bmatrix} \cdot \begin{bmatrix} \mathcal{H}_k^{trans} \\ \mathcal{H}_k^{rot} \end{bmatrix}, \quad \mathcal{C}^J = \sum_{i=1}^{N_J} \sum_{k=2}^{J_i} \begin{bmatrix} \mathbf{J}_{i,k}^n \\ \mathbf{J}_{i,k}^m \end{bmatrix} \cdot \begin{bmatrix} \mathcal{J}_{i,k}^{trans} \\ \mathcal{J}_{i,k}^{rot} \end{bmatrix}. \quad (46)$$

Here $((\boldsymbol{\lambda}, \boldsymbol{\mu}), (\mathbf{h}_k^n, \mathbf{h}_k^m), (\mathbf{J}_{i,k}^n, \mathbf{J}_{i,k}^m))$ are the three sets of unknown Lagrange multipliers to enforce global constraint, helical boundary constraint and internal joint constraints, respectively. The first variation of the above functional is obtained by varying the unknowns as follows:

$$\begin{aligned} \mathbf{r}_\epsilon^\alpha(s) &= \mathbf{r}^\alpha(s^\alpha) + \epsilon \delta \mathbf{r}^\alpha(s^\alpha), & \mathbf{R}_\epsilon^\alpha(s^\alpha) &= e^{\epsilon \delta \boldsymbol{\Theta}^\alpha(s^\alpha)} \mathbf{R}^\alpha(s^\alpha), \\ \boldsymbol{\lambda}_\epsilon &= \boldsymbol{\lambda} + \epsilon \delta \boldsymbol{\lambda}, & \boldsymbol{\mu}_\epsilon &= \boldsymbol{\mu} + \epsilon \delta \boldsymbol{\mu}, \\ \mathbf{h}_k^n &= \mathbf{h}_k^n + \epsilon \delta \mathbf{h}_k^n, & \mathbf{h}_k^m &= \mathbf{h}_k^m + \epsilon \delta \mathbf{h}_k^m, \\ \mathbf{J}_{i,k}^n &= \mathbf{J}_{i,k}^n + \epsilon \delta \mathbf{J}_{i,k}^n, & \mathbf{J}_{i,k}^m &= \mathbf{J}_{i,k}^m + \epsilon \delta \mathbf{J}_{i,k}^m. \end{aligned} \quad (47)$$

For the variation of constraint terms in (46), we refer the readers to [Appendix B](#). The first variation of the constrained energy functional for prescribed macroscopic strains $(\mathbf{v}_0^M, \mathbf{k}_0^M)$ yields the following weak form:

$$\begin{aligned} G &\equiv \frac{d}{d\epsilon} \mathcal{E}^{cons} = \frac{d\mathcal{E}^{RVE}}{d\epsilon} + \frac{d\mathcal{C}^G}{d\epsilon} + \frac{d\mathcal{C}^H}{d\epsilon} + \frac{d\mathcal{C}^J}{d\epsilon} = 0 \\ &\equiv \sum_{\alpha=1}^{N_{rods}} \int_0^{L^\alpha} (\mathbf{n}^\alpha \cdot (\delta \mathbf{r}^\alpha)' + (\mathbf{n}^\alpha \times (\mathbf{r}^\alpha)') \cdot \delta \boldsymbol{\theta}^\alpha + \mathbf{m}^\alpha \cdot (\delta \boldsymbol{\theta}^\alpha)') ds^\alpha \end{aligned}$$

⁶Although the change in rotation is being measured here with respect to a fixed reference state, the same could also be measured with respect to a converged solution, say the solution in the previous load step.

$$\begin{aligned}
& + \sum_{k=1}^{N_B} \begin{bmatrix} \boldsymbol{\lambda} \\ \boldsymbol{\Xi}_{\beta_k}^{\boldsymbol{\theta}, \alpha_k} \boldsymbol{\mu} \end{bmatrix} \begin{bmatrix} \delta \mathbf{r}_{\beta_k}^{\alpha_k} \\ \delta \boldsymbol{\theta}_{\beta_k}^{\alpha_k} \end{bmatrix} + \begin{bmatrix} \mathcal{G}^{trans} \\ \mathcal{G}^{rot} \end{bmatrix} \cdot \begin{bmatrix} \delta \boldsymbol{\lambda} \\ \delta \boldsymbol{\mu} \end{bmatrix} \\
& + \sum_{k=1}^{N_H} \left\{ \begin{bmatrix} \mathcal{H}_k^{trans} \\ \mathcal{H}_k^{rot} \end{bmatrix} \cdot \begin{bmatrix} \delta \mathbf{h}_k^n \\ \delta \mathbf{h}_k^m \end{bmatrix} + \begin{bmatrix} -\mathbf{R}_{\beta_{k_r}}^{\alpha_{k_r}} \mathbf{T}^T (\mathcal{H}_k^{rot}) \mathbf{h}_k^m \\ (\mathbf{R}^M)^T \mathbf{R}_{\beta_{k_r}}^{\alpha_{k_r}} \mathbf{T}^T (\mathcal{H}_k^{rot}) \mathbf{h}_k^m \end{bmatrix} \cdot \begin{bmatrix} \delta \mathbf{r}_{\beta_{k_r}}^{\alpha_{k_r}} \\ \delta \boldsymbol{\theta}_{\beta_{k_r}}^{\alpha_{k_r}} \end{bmatrix} \right. \\
& \quad \left. + \begin{bmatrix} -(\mathbf{R}^M)^T \mathbf{h}_k^n \\ (\mathbf{R}^M)^T \mathbf{R}_{\beta_{k_r}}^{\alpha_{k_r}} \mathbf{T}^T (\mathcal{H}_k^{rot}) \mathbf{h}_k^m \end{bmatrix} \cdot \begin{bmatrix} \delta \mathbf{r}_{\beta_k}^{\alpha_k} \\ \delta \boldsymbol{\theta}_{\beta_k}^{\alpha_k} \end{bmatrix} \right\} \\
& + \sum_{i=1}^{N_J} \sum_{k=2}^{J_i} \left\{ \begin{bmatrix} \mathcal{J}_{i,k}^{trans} \\ \mathcal{J}_{i,k}^{rot} \end{bmatrix} \cdot \begin{bmatrix} \delta \mathbf{J}_{i,k}^n \\ \delta \mathbf{J}_{i,k}^m \end{bmatrix} + \begin{bmatrix} \mathbf{J}_{i,k}^n \\ [\mathbf{R}_k \mathbf{T}^T (\mathcal{J}_{i,k}^{rot})] \mathbf{J}_{i,k}^m \end{bmatrix} \cdot \begin{bmatrix} \delta \mathbf{r}_{\beta_1}^{\alpha_1} \\ \delta \boldsymbol{\theta}_{\beta_1}^{\alpha_1} \end{bmatrix} \right. \\
& \quad \left. + \begin{bmatrix} -\mathbf{J}_{i,k}^n \\ -[\mathbf{R}_{\beta_k}^{\alpha_k} \mathbf{T}^T (\mathcal{J}_{i,k}^{rot})] \mathbf{J}_{i,k}^m \end{bmatrix} \cdot \begin{bmatrix} \delta \mathbf{r}_{\beta_k}^{\alpha_k} \\ \delta \boldsymbol{\theta}_{\beta_k}^{\alpha_k} \end{bmatrix} \right\} = 0. \tag{48}
\end{aligned}$$

In order to obtain the Euler-Lagrange equations, one simply needs to do integration by parts in the integral terms above. This will yield the usual balance equations (see equation (9)) for every rod in the RVE along with boundary load and boundary couple at the two ends of every rod. The boundary loads and boundary couples will also depend on the unknown Lagrange multipliers for which the earlier derived joint constraint, helical boundary constraint and global constraint equations will be required. The weak form (48) takes care of all of these by the way which could be suitably discretized and solved using standard numerical solvers. The rod energy of each constituent rod within the RVE is approximated using a discrete rod formulation which we have described in section 7. After solving the weak form (48), we obtain the solution of the RVE warping problem in (20) and the rod's energy density can then be written as

$$\Phi^M(\mathbf{v}_0^M, \mathbf{k}_0^M) = \frac{1}{L} \mathcal{E}^{RVE} \left(\tilde{\mathbf{r}}^\alpha(\mathbf{v}_0^M, \mathbf{k}_0^M), \tilde{\boldsymbol{\theta}}^\alpha(\mathbf{v}_0^M, \mathbf{k}_0^M) \right) \tag{49}$$

where $\{\tilde{\mathbf{r}}^\alpha(\mathbf{v}_0^M, \mathbf{k}_0^M), \tilde{\boldsymbol{\theta}}^\alpha(\mathbf{v}_0^M, \mathbf{k}_0^M)\}_{\alpha=1}^{N_{rods}}$ denotes configuration of the RVE at equilibrium. As the constraints get automatically satisfied at equilibrium, one can also write

$$\Phi^M(\mathbf{v}_0^M, \mathbf{k}_0^M) = \frac{1}{L} \tilde{\mathcal{E}}^{cons}. \tag{50}$$

which we will use to derive expressions of macroscopic internal contact force, moment and stiffnesses in the next section. Henceforth, we omit the superscript $(\tilde{\cdot})$ for conciseness.

6. Expressions of internal contact force, moment and stiffnesses of the macroscopic rod

The macroscopic internal force and moment are given by

$$\begin{bmatrix} \mathbf{n}_0^M \\ \mathbf{m}_0^M \end{bmatrix} = \frac{\partial \Phi^M}{\partial [\mathbf{v}_0^M, \mathbf{k}_0^M]^T}. \tag{51}$$

We can substitute (50) in the above equation to obtain the partial derivatives which we denote succinctly as $\delta \equiv \frac{\partial}{\partial p^M}$ where $p^M \in \{v_1^M, v_2^M, v_3^M, \kappa_1^M, \kappa_2^M, \kappa_3^M\}$. First, using (45),

we obtain

$$\begin{aligned}
\delta\mathcal{E}^{cons} = & \sum_{\alpha=1}^{N_{rods}} \int_0^{L^\alpha} (\mathbf{n}^\alpha \cdot (\delta\mathbf{r}^\alpha)' + (\mathbf{n}^\alpha \times (\mathbf{r}^\alpha)') \cdot \delta\boldsymbol{\theta}^\alpha + \mathbf{m}^\alpha \cdot (\delta\boldsymbol{\theta}^\alpha)') ds^\alpha \\
& + \sum_{k=1}^{N_B} \begin{bmatrix} \boldsymbol{\lambda} \\ \boldsymbol{\Xi}_{\beta_k}^{\theta, \alpha_k} \boldsymbol{\mu} \end{bmatrix} \begin{bmatrix} \delta\mathbf{r}_{\beta_k}^{\alpha_k} \\ \delta\boldsymbol{\theta}_{\beta_k}^{\alpha_k} \end{bmatrix} + \begin{bmatrix} \boldsymbol{\mathcal{G}}^{trans} \\ \boldsymbol{\mathcal{G}}^{rot} \end{bmatrix} \cdot \begin{bmatrix} \delta\boldsymbol{\lambda} \\ \delta\boldsymbol{\mu} \end{bmatrix} \\
& + \sum_{k=1}^{N_H} \left\{ \begin{bmatrix} \boldsymbol{\mathcal{H}}_k^{trans} \\ \boldsymbol{\mathcal{H}}_k^{rot} \end{bmatrix} \cdot \begin{bmatrix} \delta\mathbf{h}_k^n \\ \delta\mathbf{h}_k^m \end{bmatrix} + \begin{bmatrix} \mathbf{h}_k^n \\ -\mathbf{R}_{\beta_{k_r}}^{\alpha_{k_r}} \mathbf{T}^T (\boldsymbol{\mathcal{H}}_k^{rot}) \mathbf{h}_k^m \end{bmatrix} \cdot \begin{bmatrix} \delta\mathbf{r}_{\beta_{k_r}}^{\alpha_{k_r}} \\ \delta\boldsymbol{\theta}_{\beta_{k_r}}^{\alpha_{k_r}} \end{bmatrix} \right. \\
& + \begin{bmatrix} -(\mathbf{R}^M)^T \mathbf{h}_k^n \\ (\mathbf{R}^M)^T \mathbf{R}_{\beta_{k_r}}^{\alpha_{k_r}} \mathbf{T}^T (\boldsymbol{\mathcal{H}}_k^{rot}) \mathbf{h}_k^m \end{bmatrix} \cdot \begin{bmatrix} \delta\mathbf{r}_{\beta_k}^{\alpha_k} \\ \delta\boldsymbol{\theta}_{\beta_k}^{\alpha_k} \end{bmatrix} \\
& + \left. \begin{bmatrix} -\mathbf{h}_k^n \\ \mathbf{h}_k^m \end{bmatrix} \cdot \left[\begin{pmatrix} \int_0^L \delta\mathbf{R}^M(l) dl \\ \mathbf{T}(\boldsymbol{\mathcal{H}}_k^{rot}) (\mathbf{R}_{\beta_{k_r}}^{\alpha_{k_r}})^T \text{axial}(\delta\mathbf{R}^M \mathbf{R}^{M,T}) \end{pmatrix} \mathbf{v}_0^M + \int_0^L \mathbf{R}^M(l) dl \delta\mathbf{v}_0^M + \delta\mathbf{R}^M(L) \mathbf{r}_{\beta_k}^{\alpha_k} \right] \right\} \\
& + \sum_{i=1}^{N_J} \sum_{k=2}^{J_i} \left\{ \begin{bmatrix} \boldsymbol{\mathcal{J}}_k^{trans} \\ \boldsymbol{\mathcal{J}}_k^{rot} \end{bmatrix} \cdot \begin{bmatrix} \delta\mathbf{J}_k^n \\ \delta\mathbf{J}_k^m \end{bmatrix} + \begin{bmatrix} \mathbf{J}_{i,k}^n \\ \mathbf{R}_{\beta_k}^{\alpha_k} \mathbf{T}^T (\boldsymbol{\mathcal{J}}_{i,k}^{rot}) \end{bmatrix} \cdot \begin{bmatrix} \delta\mathbf{r}_{\beta_1}^{\alpha_1} \\ \delta\boldsymbol{\theta}_{\beta_1}^{\alpha_1} \end{bmatrix} \right. \\
& - \left. \begin{bmatrix} \mathbf{J}_{i,k}^n \\ [\mathbf{R}_{\beta_k}^{\alpha_k} \mathbf{T}^T (\boldsymbol{\mathcal{J}}_{i,k}^{rot})] \mathbf{J}_{i,k}^m \end{bmatrix} \cdot \begin{bmatrix} \delta\mathbf{r}_{\beta_k}^{\alpha_k} \\ \delta\boldsymbol{\theta}_{\beta_k}^{\alpha_k} \end{bmatrix} \right\}. \tag{52}
\end{aligned}$$

Note that the above equation consists of both explicit (blue terms) and implicit (black terms) derivatives of constrained energy with respect to macroscopic strains. The explicit derivative terms arise from helical boundary constraints. The closed form expressions for the terms $\int \mathbf{R}^M dl$, $\delta\mathbf{R}^M$ and $\int \delta\mathbf{R}^M dl$, wherein $\delta = \frac{\partial}{\partial \kappa_i^M}$, can be seen in Appendix B of Kumar et al. (2016). At equilibrium, using (48), the implicit derivative terms vanish as a whole. Therefore, we get

$$\delta\mathcal{E}^{cons} = \sum_{k=1}^{N_H} \begin{bmatrix} -\mathbf{h}_k^n \\ \mathbf{h}_k^m \end{bmatrix} \cdot \left[\begin{pmatrix} \int_0^L \delta\mathbf{R}^M(l) dl \\ (\mathbf{R}_{\beta_{k_r}}^{\alpha_{k_r}})^T \text{axial}(\delta\mathbf{R}^M \mathbf{R}^{M,T}) \end{pmatrix} \mathbf{v}_0^M + \int_0^L \mathbf{R}^M(l) dl \delta\mathbf{v}_0^M + \delta\mathbf{R}^M(L) \mathbf{r}_{\beta_k}^{\alpha_k} \right]. \tag{53}$$

Using equation 50, for $\delta = \frac{\partial}{\partial v_i^M}$, we get the macroscopic internal contact force, i.e.,

$$\mathbf{n}_i^M = \frac{\partial \Phi^M}{\partial v_i^M} = -\frac{1}{L} \sum_{k=1}^{N_H} \mathbf{h}_k^n \cdot \left(\int_0^L \mathbf{R}^M(l) dl \mathbf{e}_i \right) \tag{54}$$

while for $\delta = \frac{\partial}{\partial \kappa_i^M}$, we get the macroscopic internal contact moment, i.e.,

$$\begin{aligned}
\mathbf{m}_i^M = \frac{\partial \Phi^M}{\partial \kappa_i^M} = & -\frac{1}{L} \sum_{k=1}^{N_H} \mathbf{h}_k^n \cdot \left[\left(\int_0^L \frac{\partial \mathbf{R}^M(l)}{\partial \kappa_i^M} dl \right) \mathbf{v}_0^M \right] \\
& + \frac{1}{L} \sum_{k=1}^{N_H} \left(\mathbf{R}_{\beta_{k_r}}^{\alpha_{k_r}} \mathbf{h}_k^m + \mathbf{R}^M \left(\mathbf{R}^{M,T} \mathbf{h}_k^n \times \mathbf{r}_{\beta_k}^{\alpha_k} \right) \right) \cdot \text{axial} \left(\frac{\partial \mathbf{R}^M(L)}{\partial \kappa_i^M} \mathbf{R}^{M,T} \right). \tag{55}
\end{aligned}$$

Next, in order to obtain the macroscopic stiffnesses, we simply need to further differentiate the expressions of macroscopic force and moment with respect to macroscopic strain

parameters, i.e.,

$$\mathbb{C}_0^M = \frac{\partial^2 \Phi^M}{\partial[\mathbf{v}_0^M, \mathbf{k}_0^M]^T \partial[\mathbf{v}_0^M, \mathbf{k}_0^M]^T}. \quad (56)$$

First, we differentiate the macroscopic internal force equation as follows:

$$\frac{\partial^2 \Phi^M}{\partial \mathbf{v}_i^M \partial \mathbf{v}_q^M} = -\frac{1}{L} \sum_{k=1}^{N_H} \left[\frac{\partial \mathbf{h}_k^n}{\partial \mathbf{v}_q^M} \right] \cdot \left(\int_0^L \mathbf{R}^M(l) dl \right) \mathbf{e}_i, \quad (57)$$

$$\frac{\partial^2 \Phi^M}{\partial \mathbf{v}_i^M \partial \kappa_q^M} = -\frac{1}{L} \left\{ \sum_{k=1}^{N_H} \left[\frac{\partial \mathbf{h}_k^n}{\partial \kappa_q^M} \right] \cdot \left(\int_0^L \mathbf{R}^M(l) dl \right) \mathbf{e}_i + \sum_{k=1}^{N_H} \mathbf{h}_k^n \cdot \left(\int_0^L \frac{\partial \mathbf{R}^M(l)}{\partial \kappa_q^M} dl \right) \mathbf{e}_i \right\}. \quad (58)$$

Similarly, we obtain the derivative of macroscopic internal moment as follows:

$$\begin{aligned} \frac{\partial^2 \Phi}{\partial \kappa_i^M \partial \mathbf{v}_q^M} &= \frac{1}{L} \left\{ -\sum_{k=1}^{N_H} \frac{\partial \mathbf{h}_k^n}{\partial \mathbf{v}_q^M} \cdot \left(\int_0^L \frac{\partial \mathbf{R}^M(l)}{\partial \kappa_i^M} dl \right) \mathbf{v}_0^M - \sum_{k=1}^{N_H} \mathbf{h}_k^n \cdot \left(\int_0^L \frac{\partial \mathbf{R}^M(l)}{\partial \kappa_i^M} dl \right) \mathbf{e}_q \right. \\ &+ \sum_{k=1}^{N_H} \left[\frac{\partial \boldsymbol{\theta}_{\beta_{kr}}^{\alpha_{kr}}}{\partial \mathbf{v}_q^M} \times (\mathbf{R}_{\beta_{kr}}^{\alpha_{kr}} \mathbf{h}_k^m) + \mathbf{R}_{\beta_{kr}}^{\alpha_{kr}} \frac{\partial \mathbf{h}_k^m}{\partial \mathbf{v}_q^M} \right. \\ &\left. \left. + \mathbf{R}^M \left((\mathbf{R}^M)^T \frac{\partial \mathbf{h}_k^n}{\partial \mathbf{v}_q^M} \times \mathbf{r}_{\beta_k}^{\alpha_k} + (\mathbf{R}^M)^T \mathbf{h}_k^n \times \frac{\partial \mathbf{r}_{\beta_k}^{\alpha_k}}{\partial \mathbf{v}_q^M} \right) \right] \cdot \mathbf{k}_i^M \right\}, \quad (59) \end{aligned}$$

$$\begin{aligned} \frac{\partial^2 \Phi}{\partial \kappa_i^M \partial \kappa_q^M} &= \frac{1}{L} \left\{ -\sum_{k=1}^{N_H} \frac{\partial \mathbf{h}_k^n}{\partial \kappa_q^M} \cdot \left(\int_0^L \frac{\partial \mathbf{R}^M(l)}{\partial \kappa_i^M} dl \right) \mathbf{v}_0^M - \sum_{k=1}^{N_H} \mathbf{h}_k^n \cdot \left(\int_0^L \frac{\partial \mathbf{R}^M(l)}{\partial \kappa_i^M \partial \kappa_q^M} dl \right) \mathbf{v}_0^M \right. \\ &+ \sum_{k=1}^{N_H} \left[\frac{\partial \boldsymbol{\theta}_{\beta_{kr}}^{\alpha_{kr}}}{\partial \kappa_q^M} \times (\mathbf{R}_{\beta_{kr}}^{\alpha_{kr}} \mathbf{h}_k^m) + \mathbf{R}_{\beta_{kr}}^{\alpha_{kr}} \frac{\partial \mathbf{h}_k^m}{\partial \kappa_q^M} + \frac{\partial \mathbf{R}^M}{\partial \kappa_q^M} [(\mathbf{R}^M)^T \mathbf{h}_k^n \times \mathbf{r}_{\beta_k}^{\alpha_k}] \right. \\ &+ \mathbf{R}^M \left(\frac{\partial (\mathbf{R}^M)^T}{\partial \kappa_q^M} \mathbf{h}_k^n \times \mathbf{r}_{\beta_k}^{\alpha_k} + (\mathbf{R}^M)^T \frac{\partial \mathbf{h}_k^n}{\partial \kappa_q^M} \times \mathbf{r}_{\beta_k}^{\alpha_k} + (\mathbf{R}^M)^T \mathbf{h}_k^n \times \frac{\partial \mathbf{r}_{\beta_k}^{\alpha_k}}{\partial \kappa_q^M} \right) \left. \right] \cdot \mathbf{k}_i^M \\ &+ \sum_{k=1}^{N_H} \left[\mathbf{R}_{\beta_{kr}}^{\alpha_{kr}} \mathbf{h}_k^m + \mathbf{R}^M ((\mathbf{R}^M)^T \mathbf{h}_k^n \times \mathbf{r}_{\beta_k}^{\alpha_k}) \right] \cdot \left[\text{axial} \left(\frac{\partial^2 \mathbf{R}^M}{\partial \kappa_i^M \partial \kappa_q^M} (\mathbf{R}^M)^T + \frac{\partial \mathbf{R}^M}{\partial \kappa_i^M} \frac{\partial (\mathbf{R}^M)^T}{\partial \kappa_q^M} \right) \right] \left. \right\}. \quad (60) \end{aligned}$$

The above expressions also contain the derivative of unknowns $(\mathbf{r}_{\beta_k}^{\alpha_k}, \boldsymbol{\theta}_{\beta_k}^{\alpha_k}, \mathbf{h}_k^n, \mathbf{h}_k^m)$ with respect to strain parameters, i.e., $(\frac{\partial \mathbf{h}_k^n}{\partial \mathbf{v}_q^M}, \frac{\partial \mathbf{h}_k^m}{\partial \mathbf{v}_q^M}, \frac{\partial \mathbf{h}_k^n}{\partial \kappa_q^M}, \frac{\partial \mathbf{h}_k^m}{\partial \kappa_q^M}, \frac{\partial \mathbf{r}_{\beta_k}^{\alpha_k}}{\partial \mathbf{v}_q^M}, \frac{\partial \mathbf{r}_{\beta_k}^{\alpha_k}}{\partial \kappa_q^M}, \frac{\partial \boldsymbol{\theta}_{\beta_{kr}}^{\alpha_{kr}}}{\partial \mathbf{v}_q^M}, \frac{\partial \boldsymbol{\theta}_{\beta_{kr}}^{\alpha_{kr}}}{\partial \kappa_q^M})$. They can be obtained by first taking the total derivative of the nonlinear weak form (48) with respect to strain parameters and further solving the obtained linearized weak form for the unknowns mentioned above. In the next section, we discuss a procedure to discretize the rod's energy.

7. Discrete rod formulation

In this section we present a discretization approach based on the HCB rule. It results in a locking free element and we use it to obtain the discretized weak form. The approach is similar to the $SE(3)$ framework presented in [Sonnevile et al. \(2014\)](#). A rod can be thought of as a set of discrete points with their positions $\mathbf{r} = \{\mathbf{r}_1(s_1), \mathbf{r}_2(s_2), \dots, \mathbf{r}_i(s_i), \dots, \mathbf{r}_{N+1}(s_{N+1})\}$ denoting the deformed centreline of a rod. A set of orthonormal director frames $\{\mathbf{d}_{I,1}(s_1), \mathbf{d}_{I,2}(s_2), \dots, \mathbf{d}_{I,i}(s_i), \dots, \mathbf{d}_{I,N+1}(s_{N+1})\}_{I=1}^3$ is further attached to those points to describe the orientation of deformed cross-sections (see Figure 6). The quantities $(s_1, s_2, \dots, s_{N+1})$ here are the arclength coordinates of those points which need not be equispaced. As mentioned earlier, the director frames can also be described by rotation vectors, i.e., $\boldsymbol{\theta} = \{\boldsymbol{\theta}_1, \boldsymbol{\theta}_2, \dots, \boldsymbol{\theta}_{N+1}\}$. Thus, a discrete rod can be represented by the generalized coordinate $\mathbf{x} = \{\mathbf{x}_1, \mathbf{x}_2, \dots, \mathbf{x}_{N+1}\}$ where $\mathbf{x}_i = \{\mathbf{r}_i, \boldsymbol{\theta}_i\}$. One could also view a discrete rod to be a set of N segments in which the i^{th} segment is prescribed by its two end points given by its local positions \mathbf{r}_1^i (globally \mathbf{r}_i) and \mathbf{r}_2^i (globally \mathbf{r}_{i+1}), and local cross-section orientations $\boldsymbol{\theta}_1^i$ (globally $\boldsymbol{\theta}_i$) and $\boldsymbol{\theta}_2^i$ (globally $\boldsymbol{\theta}_{i+1}$). Considering uniform

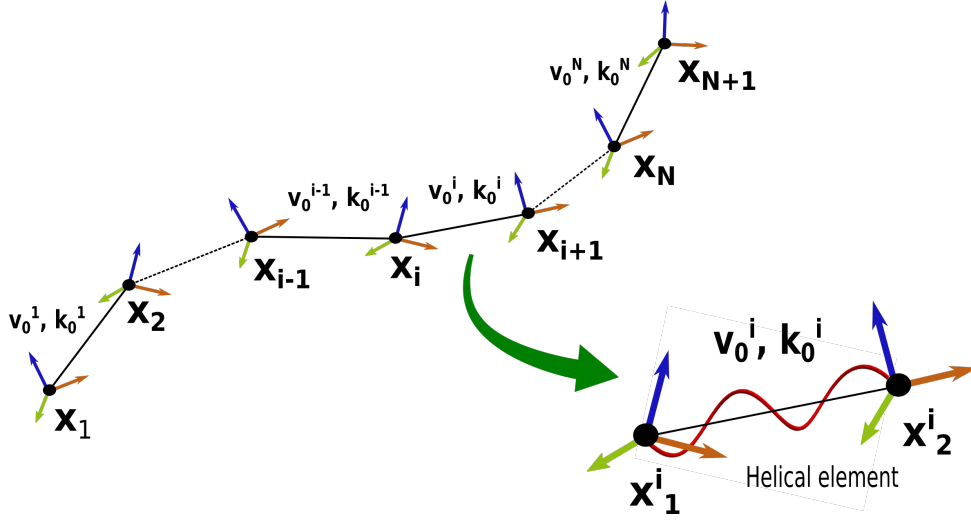


Figure 6: A schematic of a discrete helical rod: each segment is assumed to be subjected to different strain set (but uniform within the segment) making the segment helical and the entire rod as a set of distinct helices joined together.

strain field $(\mathbf{v}_0^i, \mathbf{k}_0^i)$ in the i^{th} segment, each segment becomes helical as per formula (15) due to which we also call them helical elements. The two end points of a segment then get related as follows:

$$\begin{aligned}
 \mathbf{r}_2^i &= \mathbf{r}_1^i + \mathbf{R}_1^i \left[\frac{\mathbf{v}_0^i \cdot \mathbf{k}_0^i}{\|\mathbf{k}_0^i\|^2} h^i \mathbf{k}_0^i + (\mathbf{I} - e^{h^i \mathbf{K}_0^i}) \frac{\mathbf{K}_0^i \mathbf{v}_0^i}{\|\mathbf{k}_0^i\|^2} \right] \quad (\text{see } \text{Kumar et al. (2016)}) \\
 \Rightarrow \frac{\mathbf{r}_2^i - \mathbf{r}_1^i}{h^i} &= \mathbf{R}_1^i \left[\mathbf{I} + \left(\frac{\mathbf{K}_0^i}{\|\mathbf{k}_0^i\|} \right)^2 - \left(\alpha(h^i \mathbf{k}_0^i) \mathbf{K}_0^i + \frac{\beta(h^i \mathbf{k}_0^i)}{2} h^i \mathbf{K}_0^{i2} \right) \frac{\mathbf{K}_0^i}{\|\mathbf{k}_0^i\|^2} \right] \mathbf{v}_0^i \\
 &= \mathbf{R}_1^i \left[\mathbf{I} + \frac{\beta(h^i \mathbf{k}_0^i)}{2} h^i \mathbf{K}_0^i + (1 - \alpha(h^i \mathbf{k}_0^i)) \left(\frac{\mathbf{K}_0^i}{\|\mathbf{k}_0^i\|} \right)^2 \right] \mathbf{v}_0^i \\
 &= \mathbf{R}_1^i \mathbf{T}^{-1}(h^i \mathbf{k}_0^i) \mathbf{v}_0^i \quad (\text{using (A.6)}). \tag{61}
 \end{aligned}$$

The functions $(\alpha(\cdot), \beta(\cdot))$ used in above expressions are defined in equation (A.2) while the operator $\mathbf{T}^{-1}(\cdot)$ is defined in equation (A.6) in Appendix A. We thus have

$$\mathbf{v}_0^i = \mathbf{T}(h^i \mathbf{k}_0^i) \mathbf{R}_1^{iT} \left(\frac{\mathbf{r}_2^i - \mathbf{r}_1^i}{h^i} \right). \quad (62)$$

Likewise, we have

$$\mathbf{R}_2^i = \mathbf{R}_1^i e^{h^i \mathbf{K}_0^i} \Rightarrow \mathbf{k}_0^i = \frac{1}{h^i} rv(\mathbf{R}_1^{iT} \mathbf{R}_2^i) \quad (63)$$

where rv denotes the rotation vector of corresponding rotation tensor. Having obtained the strains \mathbf{v}_0^i and \mathbf{k}_0^i in each of the rod's segments in terms of the segment's end positions and rotations using (62) and (63), we can finally write the discrete rod's energy as

$$\mathcal{I}(\mathbf{x}) = \sum_{i=1}^N \Phi(\mathbf{v}_0^i, \mathbf{k}_0^i) h^i - W^{\text{ext}} \quad (64)$$

where $\Phi(\mathbf{v}_0^i, \mathbf{k}_0^i)$ is the energy density of the discrete rod segment with strains $(\mathbf{v}_0^i, \mathbf{k}_0^i)$ and h^i is the segment's undeformed length. Likewise, W^{ext} is the work done by external loads. Analogous to the continuous setting, we minimize the discrete energy of the rod with respect to the unknown vector \mathbf{x} by setting

$$\frac{d}{d\mathbf{x}} \mathcal{I}(\mathbf{x}) = 0. \quad (65)$$

For Kirchhoff rod model where transverse shear and axial extensional strains are both zero, we model the unshearability and inextensibility constraints as follows:

$$\mathbf{v}_0^i = \mathbf{e}_3. \quad (66)$$

With the above constraint, the energy of a Kirchhoff rod can be written as

$$\mathcal{I}(\mathbf{r}, \boldsymbol{\theta}, \boldsymbol{\lambda}_0) = \sum_{i=1}^N \phi(\mathbf{k}_0^i) h^i + \sum_{i=1}^N \boldsymbol{\lambda}_0^i \cdot (\mathbf{v}_0^i - \mathbf{e}_3) - W^{\text{ext}} \quad (67)$$

where $\boldsymbol{\lambda}_0^i$ is the Lagrange multiplier vector. In case, the rod is just unshearable (but extensible), we have the following two scalar constraints:

$$\mathbf{v}_0^i \cdot \mathbf{e}_1 = 0, \quad \mathbf{v}_0^i \cdot \mathbf{e}_2 = 0. \quad (68)$$

The constrained energy functional for an unshearable rod is then given by

$$\mathcal{I}(\mathbf{r}, \boldsymbol{\theta}, \lambda_1, \lambda_2) = \sum_{i=1}^N \phi(v_3, \mathbf{k}_0^i) h^i + \sum_{i=1}^N [\lambda_1^i (\mathbf{v}_0^i \cdot \mathbf{e}_1) + \lambda_2^i (\mathbf{v}_0^i \cdot \mathbf{e}_2)] - W^{\text{ext}}. \quad (69)$$

8. Numerical examples

In this section, we solve the RVE warping problem proposed in section 5 and further obtain various macroscopic stiffnesses as detailed in section 6. An in-house code was developed on the deal.II platform (Africa et al., 2024) to solve the nonlinear RVE problem.

The main idea in this section is to study the macroscopic behavior of rod-like metamaterials formed by different types of RVEs. Each constituent rod in the RVE is modeled as a special Cosserat rod (unless otherwise mentioned). These rods are assumed to have circular cross-section and obey the strain energy function given in equation (11) wherein \mathbb{C}_0^M is taken to be a diagonal tensor with its components $\mathbb{C}_{11}^M = \mathbb{C}_{22}^M = kGA$, $\mathbb{C}_{33}^M = EA$, $\mathbb{C}_{44}^M = \mathbb{C}_{55}^M = EI$, $\mathbb{C}_{66}^M = GJ$. Here E is the Young's modulus, G is the shear modulus and k is the shear correction factor. The symbols A , I and J denote cross-sectional area, second moment of area and polar moment of area, respectively. We non-dimensionalize the RVE warping problem as follows:

$$s = \mathcal{L}\bar{s}, \quad \mathbf{r} = \mathcal{L}\bar{\mathbf{r}}, \quad \boldsymbol{\theta} = \bar{\boldsymbol{\theta}}, \quad \mathbf{k}_0 = \frac{\bar{\mathbf{k}}_0}{\mathcal{L}}, \quad \mathbf{n} = \frac{EI}{\mathcal{L}^2}\bar{\mathbf{n}}, \quad \mathbf{m} = \frac{EI}{\mathcal{L}}\bar{\mathbf{m}}. \quad (70)$$

Here the quantities with overbar, i.e., $(\bar{\cdot})$ are non-dimensionalized quantities and \mathcal{L} is the non-dimensionalization length parameter. First, we take simple planar RVEs - cross and square ones to validate the macroscopic stiffnesses obtained using the proposed formulation. Later, we take up more complex three-dimensional RVEs. In the schematics shown henceforth, we use blue color to denote the RVE and green color to denote its repetitions (shown only to the right of the RVE for visual brevity).

8.1. Cross RVE

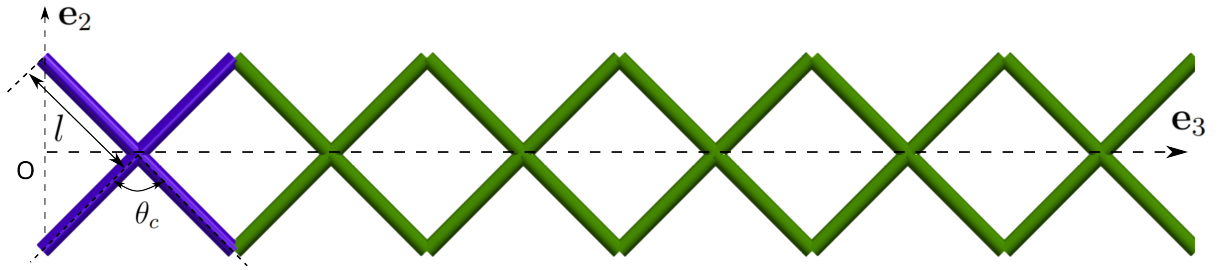


Figure 7: A rod-like metamaterial having cross-shaped RVE

Let us first consider a rod-like pantographic metamaterial (Dell'Isola and Steigmann, 2020) as shown in Figure 7. Such a metamaterial could be constructed by repeating a cross-shaped RVE in one direction. The cross RVE consists of four rods of equal length l rigidly connected to each other at the centre of the RVE. The geometric parameters of this RVE are: slenderness parameter $\frac{r}{l}$ and cross angle θ_c . For the numerical results below, we consider $\frac{r}{l} = 0.05$ and $\theta_c = \frac{\pi}{2}$. The system is non-dimensionalized by taking $\mathcal{L} = l$. We first examine the effect of including shear and extension in microscale rods on macroscopic stiffnesses. Figure 8 shows the stiffnesses at zero strain obtained using special Cosserat microscale rods - they have been normalized with their corresponding values when microscale rods are assumed Kirchhoff type, i.e., inextensible and unsharable. The formulas of the stiffnesses \mathbb{C}_{22}^M , \mathbb{C}_{33}^M and \mathbb{C}_{44}^M for the Kirchhoff case were obtained analytically in Appendix D and are also shown in Table 1. We see from Figure 8 that the effect of including shear and extension in microscale rods becomes significant at large slenderness parameter (r/l) - only the out-of-plane bending stiffness is independent of slenderness ratio. Next, we study the effect of geometric parameter θ_c on macroscopic stiffnesses at zero strain (see Figure 9). The stiffnesses have been numerically obtained for two different slenderness ratios and compared with their Kirchhoff-limit analytical formulas from Table 1. All the stiffnesses were normalized with their corresponding analytical formulas

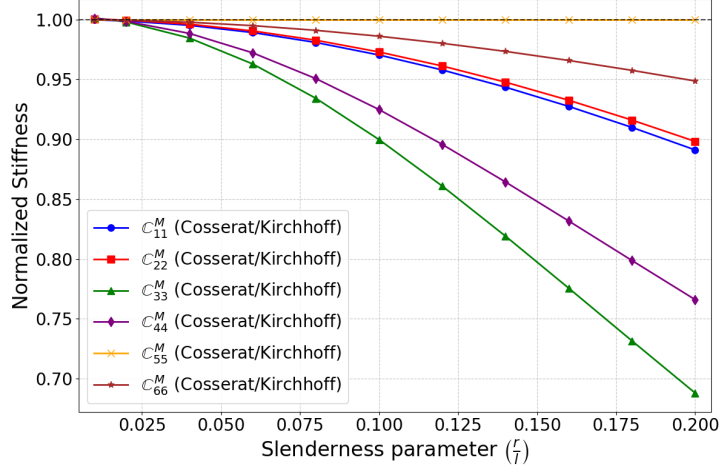


Figure 8: Cross RVE stiffnesses at zero macroscopic strain - Cosserat vs Kirchhoff constituent rods. For the Kirchhoff case, the stiffnesses C_{11}^M , C_{55}^M and C_{66}^M were obtained numerically using the present approach whereas C_{22}^M , C_{33}^M and C_{44}^M were derived analytically (see Table 1).

Table 1: Analytical formulas of stiffnesses for cross RVEs considering its constituent rods to be Kirchhoff type

C_{22}^M (in-plane shear)	C_{33}^M (extension)	C_{44}^M (in-plane bending)
$\frac{6EI}{l^2} \frac{1}{\sin \frac{\theta_c}{2}}$	$\frac{24EI}{l^2} \frac{\tan \frac{\theta_c}{2}}{\cos \frac{\theta_c}{2}}$	$8EI \sin \frac{\theta_c}{2}$

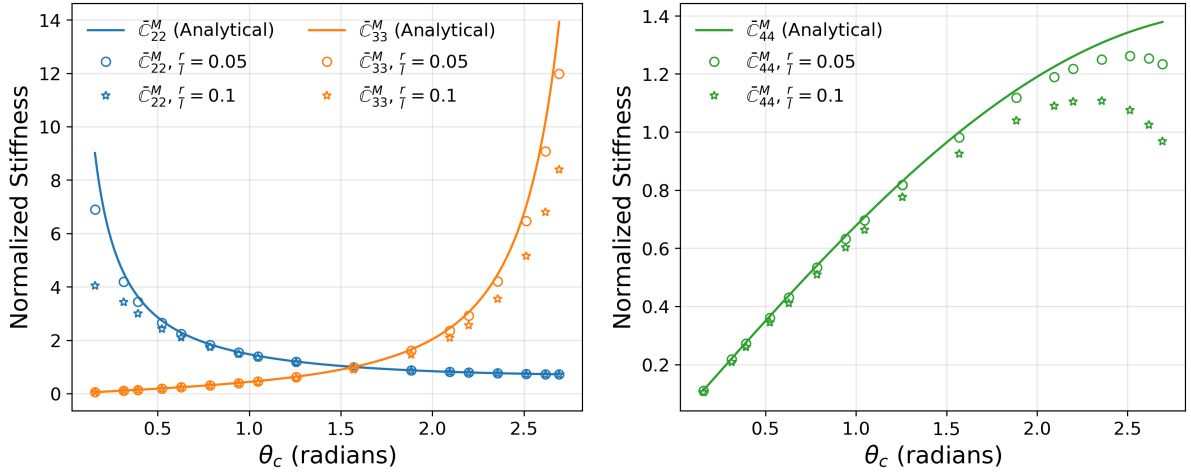


Figure 9: The variation of stiffnesses at zero strain vs. the cross-RVE parameter θ_c

at $\theta_c = \pi/2$. We note that the in-plane shearing stiffness approaches infinity as $\theta_c \rightarrow 0$ - this is because microscopic deformation due to macroscopic shearing is stretching dominated in this regime. For the same reason, macroscopic extensional stiffness approaches infinity as $\theta_c \rightarrow \pi$. Finally, as expected, the three macroscopic stiffnesses match with the analytical formulas more for smaller slenderness ratio of constituent microscale rods. We then study finite stretching of this RVE. Figure 10 shows the axial force versus axial stretch response of a uniformly stretched cross-RVE for different r/l ratios. We see that as the RVE is stretched, initially the deformation mode of microscale rods is bending dominated. Later, as the microscale rods get aligned with the macroscopic stretching direction, the deformation mode of microscale rods transitions to being stretching dom-

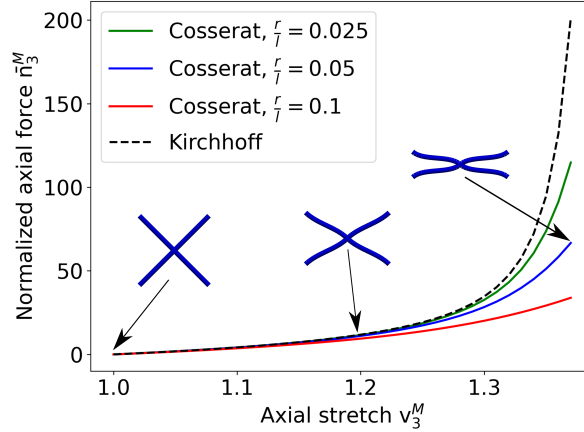


Figure 10: Finite stretching of cross-RVEs: deformation within the RVE transitions from being bending dominated to stretch dominated as seen from the insets of the RVE at different macroscopic stretch

inated. This leads to a J-shaped response as depicted in the figure. In addition, it can be seen that as the initial deformation is primarily bending-dominated, the slenderness parameter $\frac{r}{l}$ does not influence the initial macroscopic response. However, once the behavior enters stretching-dominated regime, the impact of $\frac{r}{l}$ becomes pronounced. Next,

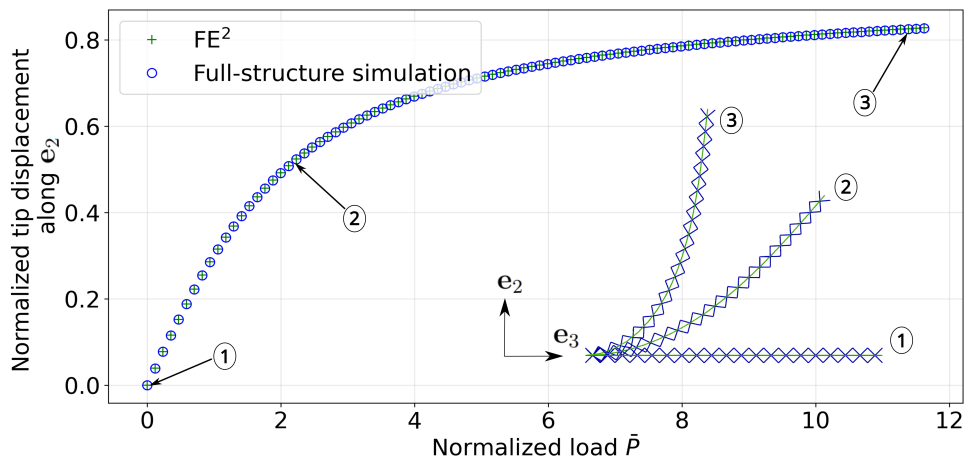


Figure 11: A comparison between FE^2 versus full-scale simulation for a cross-RVE based metamaterial. The inset shows the deformed configurations of both the full-structure (blue) and the homogenized rod depicted by its centerline (green).

we compare the full scale simulation of a cross-RVE metamaterial with the simulation of a homogenized single rod in an FE^2 framework wherein the rod's finite strain constitutive relationship is obtained using the presented homogenization scheme - see Figure 11. The metamaterial is formed by assembling 20 RVEs along \mathbf{e}_3 direction resulting in a structure of length $L_{full} = 20L$. The boundary condition of the problem is as follows: left end ($s = 0$) is clamped while at the right end ($s = L_{full}$), a concentrated normalized transverse force $\bar{\mathbf{F}} = \bar{P}\mathbf{e}_2 = P/(\mathbb{C}_{44}^M/L_{full}^2)\mathbf{e}_2$ is applied where P is the magnitude of load and \mathbb{C}_{44}^M is the macroscopic bending stiffness of the cross-RVE at zero strain. In the full structure simulation, this load is divided equally among the two nodes at the end of the metamaterial. We see a good agreement between the full scale simulation and the FE^2 approach validating our homogenization scheme.

Finally, we illustrate the effect of including non-linearity in the homogenized constitutive

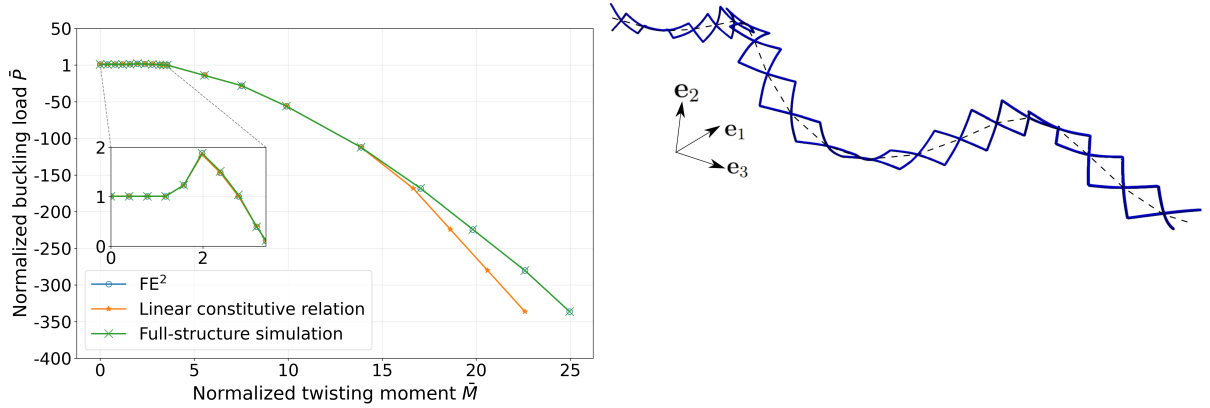


Figure 12: Variation of buckling load of a cross-RVE metamaterial in presence of twisting moment. On the right, the buckled mode shape is also shown whose centerline is non-planar due to the presence of twisting moment. The inset shows the increase in the buckling load due to bending anisotropy of cross RVEs.

relationship. To this end, we consider the problem of Euler buckling of this metamaterial in the presence of twisting moment - see Figure 12. The Euler buckling load for a clamped-free untwisted Kirchhoff rod is given by $P_{cr} = \frac{\pi^2 C_{44}^M}{4L_{full}^2}$ which is used for normalization here. The boundary condition of this problem is as follows: left end ($s = 0$) is clamped while at the right end ($s = L_{full}$), a concentrated axial compressive force $\bar{P} = P/P_{cr}$ and a twisting moment $\bar{M} = M/(P_{cr} L_{full})$ is applied. We notice that at zero twisting moment, the normalized buckling load is unity. However, the buckling load reduces as twisting moment is increased and, in fact, becomes tensile when the applied twisting moment is large enough. We again notice that the buckling load obtained using full-structure simulation matches pretty well with FE^2 simulation even at large twisting moment. However, when we use linear constitutive relation, i.e, the homogenized rod's stiffnesses (obtained at zero strain using the present approach) are not changed as the rod deforms, the curve shows deviation from full-structure simulation at large twisting moment. It is also interesting to note the initial increase in buckling load (see the inset of Figure 12). This is a classical result which is attributed to anisotropy in bending deformation. At zero twisting moment, buckling happens in the easy-bending plane. However, as the rod is twisted, no such easy bending plane exists globally and hence the buckling load increases initially.

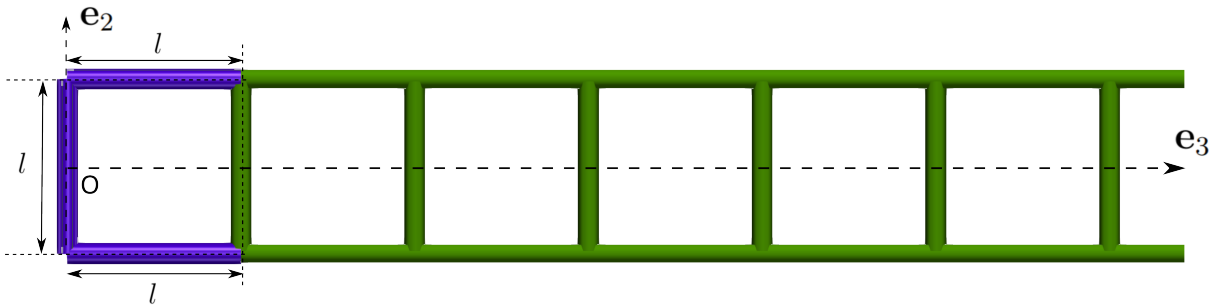


Figure 13: A square-periodic rod-like metamaterial

8.2. Square RVEs

In this section, we consider a square-periodic beam. The RVE of this beam consists of three rods of equal length l as shown in blue Figure 13. The only geometric parameter of this square RVE is its constituent rod's slenderness parameter $\frac{r}{l}$. The system is non-dimensionalized by taking $\mathcal{L} = l$. Let us study the effect of including shear deformation in microscopic rods on effective macroscopic stiffnesses. Figure 14 shows the macroscopic stiffnesses normalized by their corresponding values when the microscale rods are assumed unshearable.⁷ The derived analytical formulas for the latter case is shown in Table 2. Note from Figure 14 that the macroscopic stretching and bending stiffnesses remain unaffected by shearing of microscale rods. However, the in-plane shearing stiffness is affected significantly. Audoly and Lestringant (2023); Abdoul-Anziz and Seppecher (2018) also obtained the expression for macroscopic shearing stiffness assuming constituent rods to be unshearable (see Table 2).

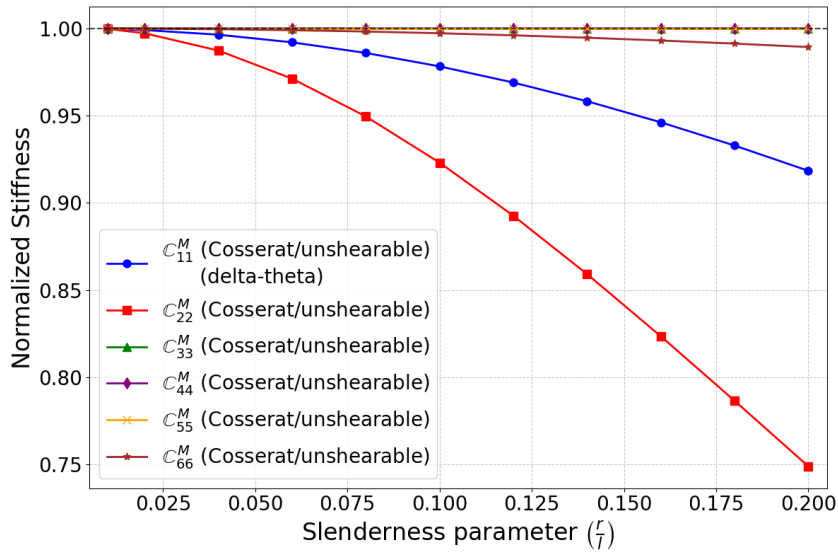


Figure 14: Normalized stiffnesses vs slenderness parameter $\frac{r}{l}$ of microscale rods in a square RVE. Here, except C_{11}^M , all stiffnesses are obtained using “mmt” constraint on corner nodes only.

Table 2: Analytical formulas of stiffnesses for square RVEs assuming constituent rods to be unshearable: the formula of C_{22}^M were taken from Audoly and Lestringant (2023); Abdoul-Anziz and Seppecher (2018) whereas other formulas were obtained analytically.

C_{22}^M (in-plane shear)	C_{33}^M (extension)	C_{44}^M (in-plane bending)	C_{55}^M (out-of-plane bending)
$\frac{8EI}{l^2}$	$2EA$	$\frac{EA l^2}{2} + 2EI$	$2EI$

8.3. Square RVEs comprising of helical rods

In this example, we take inspiration from the biophysical world. The mechanics of cytoskeletal networks present in cells has been an important field of study by researchers

⁷Unlike the cross RVE case where the microscopic rods could also be made Kirchhoff-type, we can, at best, simplify the microscale rods in square RVE case to be unshearable type only because a Kirchhoff microscale rod will lead to locking behavior when we impose macroscopic stretching or bending.

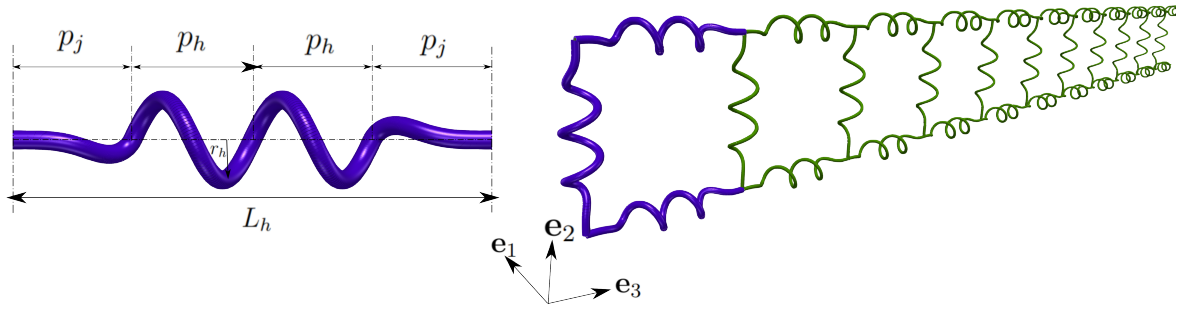


Figure 15: A rod-like metamaterial formed using square RVEs wherein the constituent rods are helical in their stress-free state (Chang et al., 2022).

(Bathe et al., 2008; Purohit et al., 2011). Such networks possess both cross-linking and folded molecular chains. Therefore, we study an idealized problem (see Figure 15) where we consider a square shaped RVE but having helical constituent rods instead of straight rods considered earlier in section 8.2. The interconnecting helical rod can be thought of as the cross-linking between two long chains. Such networks are also useful in the design of artificial tissues and muscles (Chang et al., 2022). The rods in this RVE are not strictly helical. They are composed of a uniform helix in the middle and curved rod segments at the two the ends as proposed in Chang et al. (2022). The RVE has the following geometric parameters: rod diameter d , number of turns N_h , helix pitch p_h , helix radius r_h and curved section parameter p_j as shown in Figure 15. The formula denoting the stress-free configuration of the constituent helical rod is reproduced in Appendix C. As in Chang et al. (2022), we consider the following parameter values to model each helical fiber: $N_h = 2$, $d = 0.1$, $d/r_h = 0.3$, $p_h/r_h = 3.0$, $p_j/r_h = 3.0$ in the results below unless otherwise mentioned. The non-dimensionalizing length parameter is taken to be $\mathcal{L} = L_h = 2p_j + N_h p_h$: the total end-to-end length of the helical rod. We first consider the case of stretching of this RVE. In Figure 16, the deformed configuration of the helical RVE under uniform stretching is shown. It is observed that the horizontal helical rods undergo a transition from bending-dominated to stretching-dominated behaviour. This results in low macroscopic extensional stiffness initially which gradually increases as the horizontal beams straighten and enter stretching dominated mode. Therefore, a J-shaped macroscopic response in Figure 16 is obtained. This type of response is typical of tissues (Vatankhah-Varnosfaderani et al., 2017). We also see that as the number of turns N_h is increased (keeping $\frac{d}{r_h}$, $\frac{p_h}{r_h}$, $\frac{p_j}{r_h}$ constant), the bending-dominated behaviour is prolonged and thus the transition zone of the J-shaped curve shifts towards higher stretch. Moreover, including stretching in the microscopic rod model predicts a significantly lower stiffness.

Next, the bending deformation for this RVE is studied. Figure 17 shows the normalized macroscopic bending moment \bar{m}_1^M vs the normalized macroscopic curvature. It shows the response for varying $\frac{p_h}{r_h}$ wherein r_h is kept constant and pitch is varied (the ratios $\frac{d}{r_h}$, $\frac{p_j}{r_h}$ are kept constant). The bending moment-curvature plot shows a softening behaviour. We also see that higher helix pitch value leads to higher bending moment at same curvature. This is because as the pitch increases (with constant helix radius) the helical rod becomes straighter and thus more stretching dominated, resulting in higher macroscopic bending stiffness. Moreover, the softening behaviour is achieved earlier in the case of higher pitch due to larger compressive force in the vertical rod. The larger compressive force is again

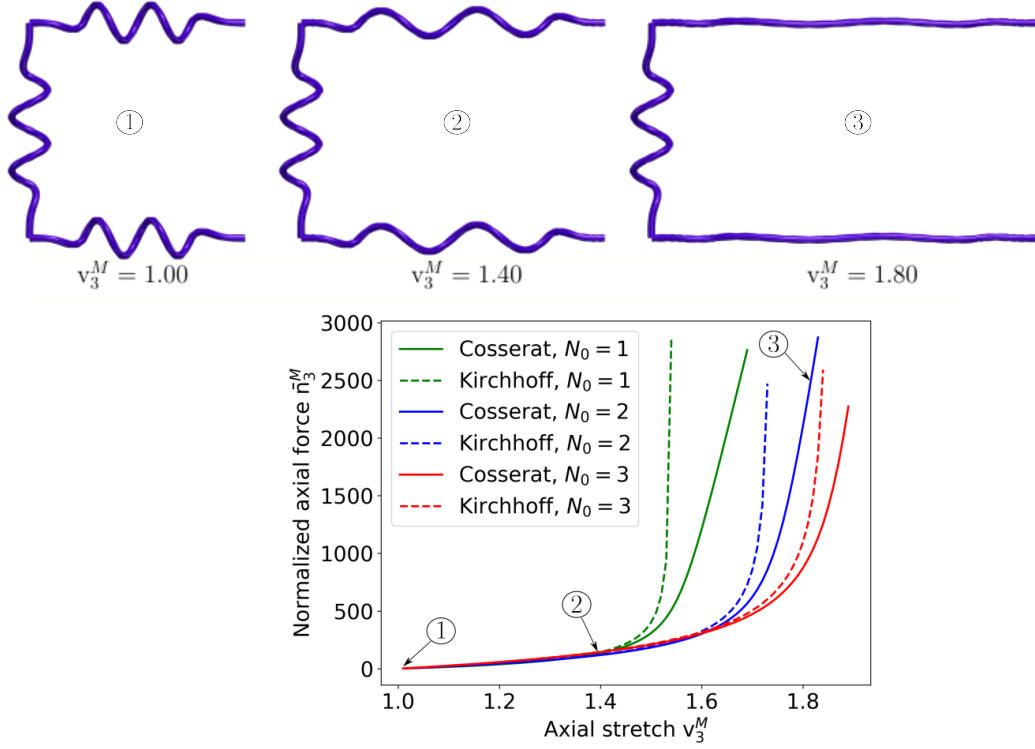


Figure 16: Uniform stretching of helical square RVEs

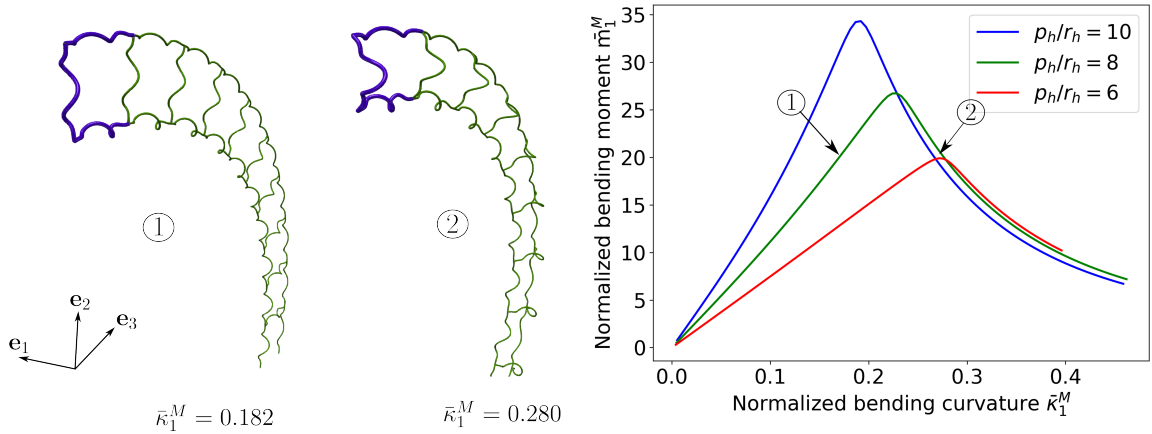


Figure 17: Pure bending of helical square RVEs ($p_h/r_h = 8.0$): at higher curvature value, the cross-linking helical rod undergoes out-of-plane bending leading to softening in macroscopic bending response.

because of the higher stretching dominated behaviour at larger pitch as discussed earlier. Figure 17 shows that the cause of the softening behaviour is the out-of-plane bending of the connecting/cross-linking helical rod. The direction of this out-of-plane bending is determined by the chirality of the connecting helical rod.

8.4. Auxetic tubular structures

Hollow auxetic rod-like or tubular structures have found use in several applications such as fasteners, stents, energy absorbing devices etc. (Tambača et al., 2010; Luo et al., 2021; Zhang et al., 2021). Some of the important mechanical characteristics of such tubular structures are their radial stiffness, flexural compliance, foreshortening etc. In case of vascular stents, these properties play an important role in dealing with clinical

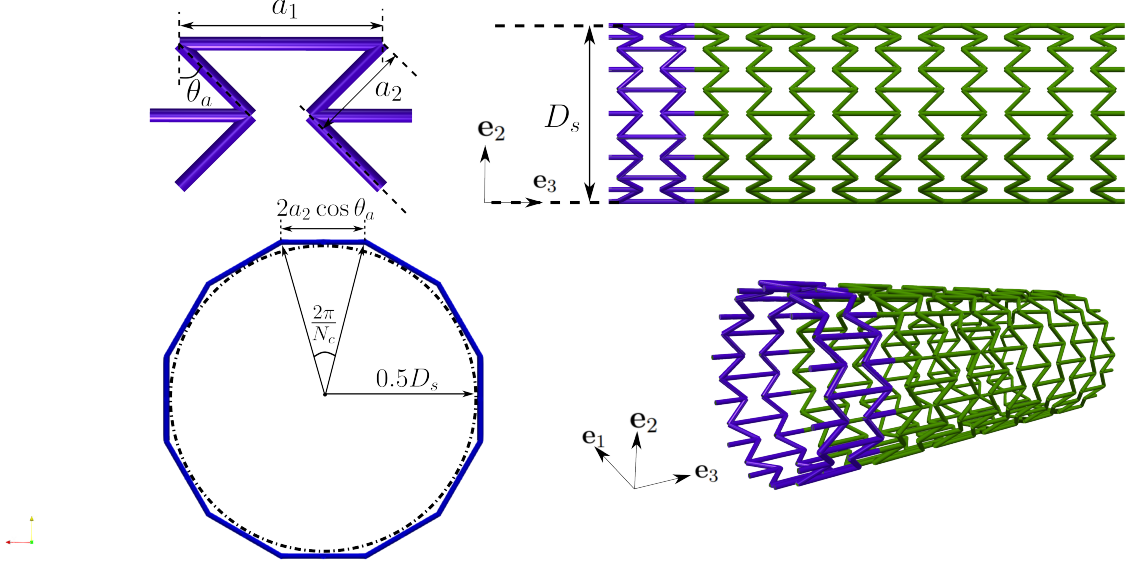


Figure 18: A tubular metamaterial constructed using auxetic unit cells (Karnesis and Burriesci, 2013).

issues such as in-stent restenosis or stent thrombosis (Pan et al., 2021; Ebrahimi et al., 2023). Moreover, such structures may undergo large three-dimensional deformation such as in the case of femoral stents (MacTaggart et al., 2014). Prithipaul et al. (2018) obtained effective stents metrics, such as foreshortening, elastic recoil and radial stiffness, by expressing periodic boundary conditions in cylindrical coordinate system for a stent undergoing only small radial expansion. In this section, we consider a tubular metamaterial that is constructed by repeating an auxetic unit cell along the circumference of a cylinder of diameter D_s (see Figure 18). Such geometry has been shown to not only result in favourable mechanical behaviour, they also integrate better with the surrounding auxetic tissues (Bhullar et al., 2013). The geometric parameters of the auxetic tubular RVE are: microscopic rod diameter d , tube diameter (in an average sense) D_s , number of unit cells along the circumference N_c , auxeticity angle θ_a , side lengths a_1 and a_2 . For the numerical results we consider the following values: $N_c = 12$, $D_s = 1.0$, $\theta_a = 30^\circ$, $d/D_s = 0.02$, $\frac{a_1}{a_2} = 1.5$. Note that, since the RVE is constructed by simply repeating the auxetic unit cell along the circumference, the length a_2 depends on the tubular RVE's parameters D_s , N_c and auxeticity angle θ_a through the formula $a_2 = \frac{0.5D_s \tan(\pi/N_c)}{\cos(\theta_a)}$. The non-dimensionalizing length parameter is taken to be $\mathcal{L} = \frac{\pi D_s}{N_c}$. We first study the effect of angle θ_a on the stent's macroscopic bending stiffness, Poisson's ratio and radial stiffness. A low bending stiffness but high radial stiffness are the desired properties of cardiovascular stents (Han and Lu, 2018). Figure 19 (left) shows the effect of angle θ_a on the macroscopic bending stiffness. We observe that the bending stiffness achieves a minima around $\theta_a = 30^\circ$. Next, we compute the effective Poisson's ratio of the tubular metamaterial. The effective Poisson's ratio is computed by applying a small axial strain to the tubular RVE after which it is given by

$$\text{Effective Poisson's ratio} = -\frac{\text{radial strain}}{\text{axial strain}} = -\frac{\frac{D_s^{def} - D_s}{D_s}}{v_3^M - 1} \quad (71)$$

where D_s^{def} is the average tubular RVE diameter in the deformed configuration. Figure 19 (middle) shows the effective Poisson's ratio for different microscopic rod diameters. Note that the Poisson's ratio of a stent is representative of its foreshortening behaviour - shortening of the stent upon radial expansion. High positive foreshortening is undesirable as it might result in the stent missing its target application area. Therefore, auxetic stents are the right candidates to mitigate this behaviour. However, unbounded large negative foreshortening is also undesirable as it runs the risk of damaging blood vessels (Prithipaul et al., 2018). Therefore, one needs to tune the geometrical parameters appropriately. Next, we study the radial stiffness of this auxetic tubular metamaterial. To do so, we apply a small outward radial force F^{radial} on each node of the RVE (except the right boundary nodes). This results in an equivalent pressure on the RVE given by

$$P_{eq} = \frac{\text{Total outward radial force}}{\text{Lateral surface area}} = \frac{N_{nodes}^{RVE} F^{radial}}{\pi D_s L} \quad (72)$$

where N_{nodes}^{RVE} is the total number of nodes on which the load F^{radial} is applied. Then we measure the resulting change in average tubular structure diameter and compute the radial stiffness using the following formula:

$$\text{Radial stiffness} = \frac{\text{Equivalent pressure}}{\text{Radial strain}} = \frac{P_{eq}}{\frac{D_s^{def} - D_s}{D_s}}. \quad (73)$$

Figure 19 (right) shows the effect of angle θ_a on the radial stiffness of the tubular RVE. Finally, we study the behaviour of the tubular metamaterial under large uniform stretch-

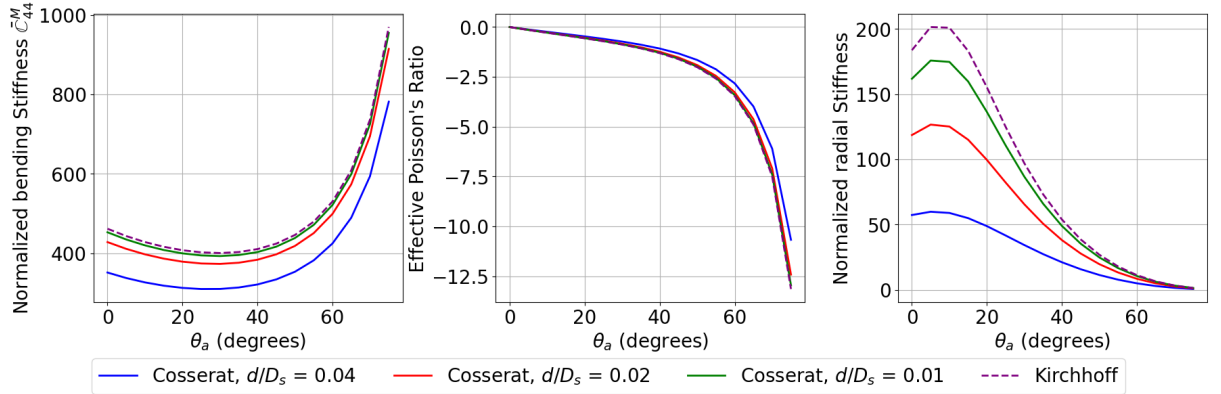


Figure 19: Normalised macroscopic properties of auxetic tubular structure vs θ_a : effect of microscopic rod's slenderness ratio d/D_s

ing and bending. Figure 20 (left) shows that, upon stretching, the average radius of the tubular RVE increases showing auxetic behaviour but at higher axial stretch, the effective Poisson's ratio turns positive eventually. We also see that initially the macroscopic extensional stiffness decreases and later increases. This is because the initial extension is dominated by bending of inclined rods which eventually transitions to stretching dominated. Next, upon uniform bending of a tubular metamaterial, we see that the model captures the well known Bazier's effect, i.e., ovalization of the cross-section (Coman, 2017; Kumar and Mukherjee, 2011) - see Figure 20 (right).

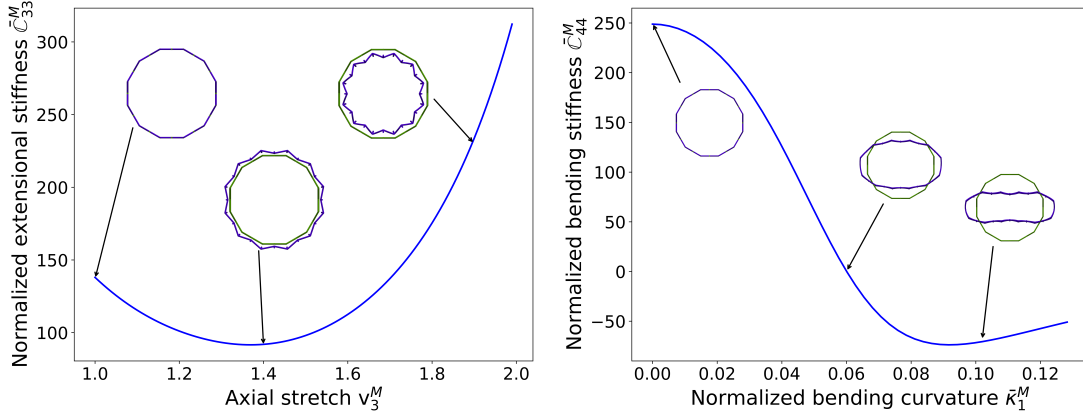


Figure 20: Uniform stretching and bending of an auxetic tubular RVE with $\theta_a = 30^\circ$

9. Conclusions

We presented a homogenization scheme to obtain the constitutive response of rod-like metamaterials when modeled as a special Cosserat rod. The HCB rule was used to strain the metamaterial uniformly (at macroscale) along its length. This, in turn, reduced the elasticity problem of entire metamaterial structure to just its RVE. The RVE problem was solved under joint constraints (to enforce rod connectivity), helical boundary constraint (to enforce helical periodicity) and a set of global constraints. The constituent/microscale rods within the RVE were also modeled using geometrically exact Cosserat rod theory. Our macro-to-micro transition map is also geometrically exact and fully nonlinear allowing the scheme to hold for arbitrarily large magnitudes of macroscopic rod's stretch, shear, curvature and twist. We also obtained closed form expressions of internal contact force, moment and stiffnesses of the rod in terms of the RVE's unknown configuration. Finally, we demonstrated our scheme using a selection of simple and complex RVEs. We began with simpler RVEs such as cross and square ones and showed that our approach results in macroscopic stiffnesses that match with the analytical expressions available in the literature and the ones derived by us. We also showed the effect of including stretch and shear modes in microscopic rods on various macroscopic stiffnesses obtained for such RVEs - shorter microscale rods showed more pronounced effect on the macroscopic response. Next, we considered square RVEs formed of helical microscale rods. We showed that its stretching results in a J-shaped curve which can be tuned by changing the RVE parameters such as the number of turns in the constituent helical rod, its pitch etc. Its bending showed unique softening behaviour in the moment vs curvature relation - this was triggered by out-of-plane bending of the cross-linking rod within the RVE. Finally, we did homogenization of auxetic tubular structures and showed how by changing its design parameters, one can obtain desirable radial stiffness, flexural compliance, foreshortening behavior etc.

In this work, we assumed the RVE to be a rod network itself. This has resulted in a general model for homogenization of rod-like heterogenous structures having position and orientation degrees of freedom at the microscale into a special Cosserat rod. The derived helical periodic boundary condition can also be used for other RVE types such as porous/composite solids (modeled as a three dimensional continuum) or origami structures (Sharma et al., 2025) (modeled as a network of plates/shells) which may include

orientation degrees of freedom (such as in micropolar theory). Furthermore, it would be interesting to study the stability of microscale rod-network in the presence of macroscopic deformations such as bending, twisting etc. for different rod-lattices. Introducing contact as a mode of interaction within the RVE to study biological networks, spiral strands, interpenetrating lattices (Surjadi et al., 2025), etc. would also be interesting. The proposed formulation assumes arbitrary constitutive behaviour for the microscale rods. This feature can be utilized to see the effect of elastoplasticity or viscoelasticity of microscale rods on macroscopic behaviour. These inelastic effects become an important considerations for applications such as in the case of cardiovascular stents deployment, muscles actuation (Wang et al., 2023) etc. Furthermore, due to increasing interest in deployable structures, 4D printing and robotic actuators/sensors, one could also think of including multiphysics phenomena such as thermoelasticity, chemoelasticity, electroelasticity (Barceló-Mercader et al., 2024) etc. at microscale and obtain the coupled multiphysics response at macroscale. We have also assumed the macroscopic strain energy density to depend only on rod’s strains. However, in case the strain gradient along the arc-length of the macroscopic rod becomes significant, one would need to resort to higher gradient rod theory at macroscale (Yadav and Gupta, 2024). Finally, it would make sense to train a machine learning based constitutive model using data obtained from the proposed formulation and readily use such a tool in FE² setting (Schommartz et al., 2025).

References

- P. Jiao, J. Mueller, J. R. Raney, X. Zheng, A. H. Alavi, Mechanical metamaterials and beyond, *Nature communications* 14 (2023) 6004.
- P. Jiao, Mechanical energy metamaterials in interstellar travel, *Progress in Materials Science* 137 (2023) 101132.
- O. Weeger, N. Boddeti, S.-K. Yeung, S. Kaijima, M. L. Dunn, Digital design and nonlinear simulation for additive manufacturing of soft lattice structures, *Additive Manufacturing* 25 (2019) 39–49.
- N. A. Fleck, V. S. Deshpande, M. F. Ashby, Micro-architected materials: past, present and future, *Proceedings of the Royal Society A: Mathematical, Physical and Engineering Sciences* 466 (2010) 2495–2516.
- M. G. Lee, J. W. Lee, S. C. Han, K. Kang, Mechanical analyses of “shellular”, an ultralow-density material, *Acta Materialia* 103 (2016) 595–607.
- K. Krishnan, D.-W. Lee, M. Al Teneji, R. K. A. Al-Rub, Effective stiffness, strength, buckling and anisotropy of foams based on nine unique triple periodic minimal surfaces, *International Journal of Solids and Structures* 238 (2022) 111418.
- J. Chang, D. Yan, J. Liu, F. Zhang, Y. Zhang, Mechanics of three-dimensional soft network materials with a class of bio-inspired designs, *Journal of Applied Mechanics* 89 (2022) 071004.
- J. U. Surjadi, C. M. Portela, Enabling three-dimensional architected materials across length scales and timescales, *Nature Materials* (2025) 1–13.
- Y. Han, W. Lu, Optimizing the deformation behavior of stent with nonuniform poisson’s ratio distribution for curved artery, *Journal of the mechanical behavior of biomedical materials* 88 (2018) 442–452.

- J. Sun, S. Zhang, J. Deng, J. Li, D. Wang, J. Liu, Y. Liu, Recent advances in twisted and coiled artificial muscles and their applications, *SmartBot* (2025) e12005.
- A. Parra Rubio, D. Fan, B. Jenett, J. del Águila Ferrandis, F. Tournomousis, A. Abdel-Rahman, D. Preiss, J. Zemánek, M. Triantafyllou, N. Gershenfeld, Modular morphing lattices for large-scale underwater continuum robotic structures, *Soft Robotics* (2023).
- Y. Wu, H. Yao, X. Li, S. Han, Metamaterial shaft with a low poisson's ratio lattice structure for torsional vibration isolation, *Mechanical Systems and Signal Processing* 228 (2025) 112454.
- L. R. Meza, A. J. Zelhofer, N. Clarke, A. J. Mateos, D. M. Kochmann, J. R. Greer, Resilient 3d hierarchical architected metamaterials, *Proceedings of the National Academy of Sciences* 112 (2015) 11502–11507.
- W. P. Moestopo, A. J. Mateos, R. M. Fuller, J. R. Greer, C. M. Portela, Pushing and pulling on ropes: hierarchical woven materials, *Advanced Science* 7 (2020) 2001271.
- F. Emami, A. J. Gross, Warren truss inspired hierarchical beams for three dimensional hierarchical truss lattice materials, *Mechanics of Materials* (2024) 105088.
- S. Saeb, P. Steinmann, A. Javili, Aspects of computational homogenization at finite deformations: a unifying review from reuss' to voigt's bound, *Applied Mechanics Reviews* 68 (2016) 050801.
- V. S. Deshpande, N. A. Fleck, M. F. Ashby, Effective properties of the octet-truss lattice material, *Journal of the Mechanics and Physics of Solids* 49 (2001) 1747–1769.
- A. Vigliotti, D. Pasini, Linear multiscale analysis and finite element validation of stretching and bending dominated lattice materials, *Mechanics of Materials* 46 (2012a) 57–68.
- A. Vigliotti, D. Pasini, Stiffness and strength of tridimensional periodic lattices, *Computer methods in applied mechanics and engineering* 229 (2012b) 27–43.
- L. Herrnböck, P. Steinmann, Homogenization of fully nonlinear rod lattice structures: on the size of the rve and micro structural instabilities, *Computational Mechanics* 69 (2022) 947–964.
- Y. Rahali, I. Giorgio, J.-F. Ganghoffer, F. Dell'Isola, Homogenization à la piola produces second gradient continuum models for linear pantographic lattices, *International Journal of Engineering Science* 97 (2015) 148–172.
- M. G. Geers, E. W. Coenen, V. G. Kouznetsova, Multi-scale computational homogenization of structured thin sheets, *Modelling and Simulation in Materials Science and Engineering* 15 (2007) S393.
- R. N. Glaesener, C. Lestringant, B. Telgen, D. M. Kochmann, Continuum models for stretching-and bending-dominated periodic trusses undergoing finite deformations, *International Journal of Solids and Structures* 171 (2019) 117–134.
- O. Weeger, Numerical homogenization of second gradient, linear elastic constitutive models for cubic 3d beam-lattice metamaterials, *International Journal of Solids and Structures* 224 (2021) 111037.

- P. Seppecher, J.-J. Alibert, F. D. Isola, Linear elastic trusses leading to continua with exotic mechanical interactions, in: *Journal of Physics: Conference Series*, volume 319, IOP Publishing, 2011, p. 012018.
- B. Audoly, C. Lestringant, An energy approach to asymptotic, higher-order, linear homogenization, *Journal of Theoretical, Computational and Applied Mechanics* (2023). URL: <https://hal.science/hal-04112136>. doi:10.46298/jtcam.11414.
- H. Yang, W. H. Müller, Size effects of mechanical metamaterials: a computational study based on a second-order asymptotic homogenization method, *Archive of applied mechanics* 91 (2021) 1037–1053.
- S. Alavi, J. Ganghoffer, M. Sadighi, M. Nasimsobhan, A. Akbarzadeh, Continualization method of lattice materials and analysis of size effects revisited based on cosserat models, *International Journal of Solids and Structures* 254 (2022) 111894.
- M. Sarhil, L. Scheunemann, J. Schröder, P. Neff, Size-effects of metamaterial beams subjected to pure bending: on boundary conditions and parameter identification in the relaxed micromorphic model, *Computational Mechanics* (2023) 1–23.
- S. S. Antman, Problems in nonlinear elasticity, *Nonlinear Problems of Elasticity* (2005) 513–584.
- W. Yu, D. H. Hodges, J. C. Ho, Variational asymptotic beam sectional analysis—an updated version, *International journal of engineering science* 59 (2012) 40–64.
- B. Audoly, C. Lestringant, Asymptotic derivation of high-order rod models from nonlinear 3d elasticity, *Journal of the Mechanics and Physics of Solids* 148 (2021) 104264.
- J. C. Simo, L. Vu-Quoc, A geometrically-exact rod model incorporating shear and torsion-warping deformation, *International Journal of Solids and Structures* 27 (1991) 371–393.
- M. Chadha, M. D. Todd, A comprehensive kinematic model of single-manifold cosserat beam structures with application to a finite strain measurement model for strain gauges, *International Journal of Solids and Structures* 159 (2019) 58–76.
- A. Arora, A. Kumar, P. Steinmann, A computational approach to obtain nonlinearly elastic constitutive relations of special cosserat rods, *Computer Methods in Applied Mechanics and Engineering* 350 (2019) 295–314.
- A. K. Noor, M. S. Anderson, W. H. Greene, Continuum models for beam-and platelike lattice structures, *Aiaa Journal* 16 (1978) 1219–1228.
- J. D. Renton, The beam-like behavior of space trusses, *AIAA journal* 22 (1984) 273–280.
- B. Burgardt, P. Cartraud, Continuum modeling of beamlike lattice trusses using averaging methods, *Computers & structures* 73 (1999) 267–279.
- N. B. Kahla, Equivalent beam-column analysis of guyed towers, *Computers & structures* 55 (1995) 631–645.
- S. Cao, M. Huo, N. Qi, C. Zhao, D. Zhu, L. Sun, Extended continuum model for dynamic analysis of beam-like truss structures with geometrical nonlinearity, *Aerospace Science and Technology* 103 (2020) 105927.

- F. Liu, L. Wang, D. Jin, H. Wen, Equivalent continuum modeling of beam-like truss structures with flexible joints, *Acta Mechanica Sinica* 35 (2019) 1067–1078.
- H. Abdoul-Anziz, P. Seppecher, Strain gradient and generalized continua obtained by homogenizing frame lattices, *Mathematics and mechanics of complex systems* 6 (2018) 213–250.
- F. Ménard, P. Cartraud, Solid and 3d beam finite element models for the nonlinear elastic analysis of helical strands within a computational homogenization framework, *Computers & Structures* 257 (2021) 106675.
- M. A. Saadat, D. Durville, A mixed stress-strain driven computational homogenization of spiral strands, *Computers & Structures* 279 (2023) 106981.
- A. Kumar, S. Kumar, P. Gupta, A helical cauchy-born rule for special cosserat rod modeling of nano and continuum rods, *Journal of Elasticity* 124 (2016) 81–106.
- Vinayak, et al., Uniformly strained anisotropic elastoplastic rods: determination of elastoplastic constitutive relations and yield surface in terms of rod’s variables, *European Journal of Mechanics-A/Solids* 98 (2023) 104867.
- R. Kumar, V. Agarwal, A. Kumar, A computational approach to obtain nonlinearly elastic constitutive relations of strips modeled as a special cosserat rod, *Computer Methods in Applied Mechanics and Engineering* 418 (2024) 116553.
- G. Jelenić, M. Crisfield, Non-linear ‘master-slave’relationships for joints in 3-d beams with large rotations, *Computer methods in applied mechanics and engineering* 135 (1996) 211–228.
- A. Ibrahimbegović, S. Mamouri, On rigid components and joint constraints in nonlinear dynamics of flexible multibody systems employing 3d geometrically exact beam model, *Computer Methods in Applied Mechanics and Engineering* 188 (2000) 805–831.
- K. Yeoh, L. Poh, T. Tay, V. Tan, Multiscale computational homogenisation of shear-flexible beam elements: a direct fe2 approach, *Computational Mechanics* 70 (2022) 891–910.
- S. Čanić, L. Grubišić, D. Lacmanović, M. Ljulj, J. Tambača, Optimal design of vascular stents using a network of 1d slender curved rods, *Computer methods in applied mechanics and engineering* 394 (2022) 114853.
- V. Sonnevile, A. Cardona, O. Brüls, Geometrically exact beam finite element formulated on the special euclidean group $se(3)$, *Computer Methods in Applied Mechanics and Engineering* 268 (2014) 451–474.
- P. C. Africa, D. Arndt, W. Bangerth, B. Blais, M. Fehling, R. Gassmüller, T. Heister, L. Heltai, S. Kinnewig, M. Kronbichler, M. Maier, P. Munch, M. Schreter-Fleischhacker, J. P. Thiele, B. Turcksin, D. Wells, V. Yushutin, The deal.ii library, version 9.6, *Journal of Numerical Mathematics* 32 (2024) 369–380. doi:[10.1515/jnma-2024-0137](https://doi.org/10.1515/jnma-2024-0137).
- F. Dell’Isola, D. J. Steigmann, *Discrete and continuum models for complex metamaterials*, Cambridge University Press, 2020.

- M. Bathe, C. Heussinger, M. M. Claessens, A. R. Bausch, E. Frey, Cytoskeletal bundle mechanics, *Biophysical journal* 94 (2008) 2955–2964.
- P. K. Purohit, R. I. Litvinov, A. E. Brown, D. E. Discher, J. W. Weisel, Protein unfolding accounts for the unusual mechanical behavior of fibrin networks, *Acta biomaterialia* 7 (2011) 2374–2383.
- M. Vatankhah-Varnosfaderani, W. F. Daniel, M. H. Everhart, A. A. Pandya, H. Liang, K. Matyjaszewski, A. V. Dobrynin, S. S. Sheiko, Mimicking biological stress–strain behaviour with synthetic elastomers, *Nature* 549 (2017) 497–501.
- N. Karnesis, G. Burriesci, Uniaxial and buckling mechanical response of auxetic cellular tubes, *Smart Materials and Structures* 22 (2013) 084008.
- J. Tambača, M. Kosor, S. Čanić, D. P. MD, Mathematical modeling of vascular stents, *SIAM journal on applied mathematics* 70 (2010) 1922–1952.
- C. Luo, C. Z. Han, X. Y. Zhang, X. G. Zhang, X. Ren, Y. M. Xie, Design, manufacturing and applications of auxetic tubular structures: A review, *Thin-Walled Structures* 163 (2021) 107682.
- X. Y. Zhang, X. Ren, X. Y. Wang, Y. Zhang, Y. M. Xie, A novel combined auxetic tubular structure with enhanced tunable stiffness, *Composites Part B: Engineering* 226 (2021) 109303.
- C. Pan, Y. Han, J. Lu, Structural design of vascular stents: A review, *Micromachines* 12 (2021) 770.
- M. S. Ebrahimi, M. Noruzi, R. Hamzehei, E. Etemadi, R. Hashemi, Revolutionary auxetic intravascular medical stents for angioplasty applications, *Materials & Design* 235 (2023) 112393.
- J. N. MacTaggart, N. Y. Phillips, C. S. Lomneth, I. I. Pipinos, R. Bowen, B. T. Baxter, J. Johanning, G. M. Longo, A. S. Desyatova, M. J. Moulton, et al., Three-dimensional bending, torsion and axial compression of the femoropopliteal artery during limb flexion, *Journal of biomechanics* 47 (2014) 2249–2256.
- P. K. Prithipaul, M. Kokkolaras, D. Pasini, Assessment of structural and hemodynamic performance of vascular stents modelled as periodic lattices, *Medical engineering & physics* 57 (2018) 11–18.
- S. Bhullar, A. M. Hewage, A. Alderson, K. Alderson, M. B. Jun, Influence of negative poisson’s ratio on stent applications, *Adv. Mater* 2 (2013) 42–47.
- C. D. Coman, Bifurcation instabilities in finite bending of circular cylindrical shells, *International Journal of Engineering Science* 119 (2017) 249–264.
- A. Kumar, S. Mukherjee, A geometrically exact rod model including in-plane cross-sectional deformation (2011).
- A. Sharma, S. Naskar, T. Mukhopadhyay, Programmable constitutive mode-coupling in tubular origami metamaterials, *npj Metamaterials* 1 (2025) 4.

J. U. Surjadi, B. F. Aymon, M. Carton, C. M. Portela, Double-network-inspired mechanical metamaterials, *Nature Materials* (2025) 1–10.

X. Wang, H. Shao, J. Tang, J. Chen, Y. Huang, J. Pan, Y. Zhang, W. Wang, J. Jiang, N. Chen, Braided liquid crystal elastomer fiber actuator with programmable deformation for artificial muscles, *Advanced Materials Technologies* 8 (2023) 2300814.

J. Barceló-Mercader, D. Codony, A. Mocci, I. Arias, Computational homogenization of higher-order electro-mechanical materials with built-in generalized periodicity conditions, *Computer Methods in Applied Mechanics and Engineering* 423 (2024) 116861.

V. K. Yadav, P. Gupta, A strain-gradient elastic theory for special cosserat rods, *International Journal of Solids and Structures* 291 (2024) 112696.

J. O. Schommartz, D. K. Klein, J. C. A. Cobo, O. Weeger, Physics-augmented neural networks for constitutive modeling of hyperelastic geometrically exact beams, *Computer Methods in Applied Mechanics and Engineering* 435 (2025) 117592.

J. C. Simo, L. Vu-Quoc, On the dynamics in space of rods undergoing large motions—a geometrically exact approach, *Computer methods in applied mechanics and engineering* 66 (1988) 125–161.

Appendix A. Important rotation related formulas

The Rodrigue’s formula for the rotation tensor corresponding to rotation vector $\boldsymbol{\theta}$ is given by

$$\mathbf{R}(\boldsymbol{\theta}) = e^{\boldsymbol{\Theta}} = \mathbf{I} + \alpha\boldsymbol{\Theta} + \frac{\beta}{2}\boldsymbol{\Theta}^2 \quad (\text{A.1})$$

where

$$\boldsymbol{\Theta} = \text{skew}(\boldsymbol{\theta}), \quad \alpha(\boldsymbol{\theta}) = \frac{\sin(\|\boldsymbol{\theta}\|)}{\|\boldsymbol{\theta}\|}, \quad \beta(\boldsymbol{\theta}) = 2\frac{1 - \cos(\|\boldsymbol{\theta}\|)}{\|\boldsymbol{\theta}\|^2}. \quad (\text{A.2})$$

The variation/linearization of the rotation tensor is obtained through a multiplicative perturbation in the following way:

$$\left. \frac{d}{d\epsilon} \mathbf{R}^\epsilon \right|_{\epsilon=0} = \left. \frac{d}{d\epsilon} [e^{\epsilon\delta\boldsymbol{\Theta}} \mathbf{R}] \right|_{\epsilon=0} = \delta\boldsymbol{\Theta} \mathbf{R} \quad (\text{A.3})$$

where $\delta\boldsymbol{\Theta} = \text{skew}(\delta\boldsymbol{\theta})$. Thus, we have

$$\delta\boldsymbol{\theta} = \text{axial} \left(\left. \frac{d\mathbf{R}^\epsilon}{d\epsilon} \right|_{\epsilon=0} \mathbf{R}^T \right). \quad (\text{A.4})$$

Let us denote the variation of rotation vector $\boldsymbol{\theta}$ by $\Delta\boldsymbol{\theta}$. It is related to the multiplicative perturbation $\delta\boldsymbol{\theta}$ using the following identity (Simo and Vu-Quoc, 1988):

$$\Delta\boldsymbol{\theta} = \left. \frac{d\boldsymbol{\theta}^\epsilon}{d\epsilon} \right|_{\epsilon=0} = \mathbf{T}(\boldsymbol{\theta})\delta\boldsymbol{\theta}, \quad \delta\boldsymbol{\theta} = \mathbf{T}^{-1}(\boldsymbol{\theta})\Delta\boldsymbol{\theta} \quad (\text{A.5})$$

where

$$\mathbf{T}(\boldsymbol{\theta}) = \mathbf{I} - \frac{\boldsymbol{\Theta}}{2} + (1 - \frac{\alpha}{\beta}) \left(\frac{\boldsymbol{\Theta}}{\|\boldsymbol{\theta}\|} \right)^2, \quad \mathbf{T}^{-1}(\boldsymbol{\theta}) = \mathbf{I} + \frac{\beta}{2} \boldsymbol{\Theta} + (1 - \alpha) \left(\frac{\boldsymbol{\Theta}}{\|\boldsymbol{\theta}\|} \right)^2. \quad (\text{A.6})$$

Finally, the following identity holds:

$$\mathbf{T}(\mathbf{Q}\boldsymbol{\theta}) = \mathbf{Q}\mathbf{T}(\boldsymbol{\theta})\mathbf{Q}^T \quad \text{and} \quad \mathbf{T}^{-1}(\mathbf{Q}\boldsymbol{\theta}) = \mathbf{Q}\mathbf{T}^{-1}(\boldsymbol{\theta})\mathbf{Q}^T \quad (\text{A.7})$$

where \mathbf{Q} is an arbitrary rotation tensor.

Appendix B. Linearization of various constraints

Appendix B.1. Linearization of global constraints

Let us first consider the ‘‘mmt’’ constraint in (40), i.e.,

$$\mathbf{m} = r_2 r_3 \mathbf{e}_1 + r_1 r_3 \mathbf{e}_2 + \left[\arctan\left(\frac{r_2}{r_1}\right) - \arctan\left(\frac{R_2}{R_1}\right) \right] \mathbf{e}_3. \quad (\text{B.1})$$

Here the indices (α_k, β_k) have been omitted for simplicity. The linearization of the above constraint is given by

$$\left. \frac{d\mathbf{m}}{d\epsilon} \right|_{\epsilon=0} = \boldsymbol{\Xi}^T \delta \mathbf{r} \quad (\text{B.2})$$

where

$$[\boldsymbol{\Xi}^T] = \begin{bmatrix} 0 & r_3 & r_2 \\ r_3 & 0 & r_1 \\ -\frac{r_2}{r_1^2 + r_2^2} & \frac{r_1}{r_1^2 + r_2^2} & 0 \end{bmatrix}. \quad (\text{B.3})$$

Next we obtain the linearization of ‘‘delta-theta’’ constraint in equation (43). Let us consider the change in rotation vector $\Delta\boldsymbol{\theta}$ (omitting the indices (α_k, β_k)) there and define its pull-back to the reference configuration as

$$\mathbf{R}(\boldsymbol{\theta}) = \mathbf{R}(\hat{\boldsymbol{\theta}}) \exp^{\Delta\boldsymbol{\theta}_0} \quad (\text{B.4})$$

such that

$$\Delta\boldsymbol{\theta}_0 = \hat{\mathbf{R}}^T \Delta\boldsymbol{\theta} \quad (\text{B.5})$$

Linearizing equation (B.4), further taking the axial and applying (A.5), we obtain

$$\left. \frac{d}{d\epsilon} \Delta\boldsymbol{\theta}_0^\epsilon \right|_{\epsilon=0} = \mathbf{T}(\Delta\boldsymbol{\theta}_0) \hat{\mathbf{R}}^T \delta\boldsymbol{\theta}. \quad (\text{B.6})$$

Using (B.5) and (A.7), we finally have the linearization of change in rotation vector as follows:

$$\left. \frac{d}{d\epsilon} \Delta\boldsymbol{\theta}^\epsilon \right|_{\epsilon=0} = \hat{\mathbf{R}} \mathbf{T}(\Delta\boldsymbol{\theta}_0) \hat{\mathbf{R}}^T \delta\boldsymbol{\theta} = \mathbf{T}(\Delta\boldsymbol{\theta}) \delta\boldsymbol{\theta} = \boldsymbol{\Xi}^{\theta^T} \delta\boldsymbol{\theta} \quad (\text{B.7})$$

where

$$\Xi^{\theta^T} = \mathbf{T}(\Delta\theta). \quad (\text{B.8})$$

Appendix B.2. Linearization of internal joint constraints

In this section, we derive the linearization of internal joint rotational constraint term. In order to do so, we first define the constraint in (26) as

$$\mathcal{J}_{i,k}^{rot} \equiv \theta_{i,k}^{rel} = \mathbf{0} \quad (\text{B.9})$$

where $\theta_{i,k}^{rel}$ is the relative rotation vector. It is defined using the left multiplicative update as

$$(\mathbf{R}_{\beta_k}^{\alpha_k})^T \mathbf{R}_{\beta_1}^{\alpha_1} = e^{\Theta_{i,k}^{rel}} (\hat{\mathbf{R}}_{\beta_k}^{\alpha_k})^T \hat{\mathbf{R}}_{\beta_1}^{\alpha_1} \quad (\text{B.10})$$

or using the right multiplicative update as

$$(\mathbf{R}_{\beta_k}^{\alpha_k})^T \mathbf{R}_{\beta_1}^{\alpha_1} = (\hat{\mathbf{R}}_{\beta_k}^{\alpha_k})^T \hat{\mathbf{R}}_{\beta_1}^{\alpha_1} e^{\Theta_{0,i,k}^{rel}} \quad (\text{B.11})$$

such that

$$\theta_{i,k}^{rel} = (\hat{\mathbf{R}}_{\beta_k}^{\alpha_k})^T \hat{\mathbf{R}}_{\beta_1}^{\alpha_1} \theta_{0,i,k}^{rel}. \quad (\text{B.12})$$

Then the linearization of the rotational internal joint constraint (26) is given by

$$\left. \frac{d}{d\epsilon} \mathcal{J}_{i,k}^{rot} \right|_{\epsilon=0} = \left. \frac{d\theta_{i,k}^{rel}}{d\epsilon} \right|_{\epsilon=0}. \quad (\text{B.13})$$

Now, we linearize equation (B.11), take its *axial* on both the sides and use (A.5) to obtain

$$(\mathbf{R}_{\beta_k}^{\alpha_k})^T (\delta\theta_{\beta_1}^{\alpha_1} - \delta\theta_{\beta_k}^{\alpha_k}) = (\hat{\mathbf{R}}_{\beta_k}^{\alpha_k})^T \hat{\mathbf{R}}_{\beta_1}^{\alpha_1} \mathbf{T}^{-1}(\theta_{0,i,k}^{rel}) \left. \frac{d\theta_{0,i,k}^{rel}}{d\epsilon} \right|_{\epsilon=0}. \quad (\text{B.14})$$

Finally, using (B.12) and (A.7), we get

$$\left. \frac{d\theta_{i,k}^{rel}}{d\epsilon} \right|_{\epsilon=0} = \mathbf{T}(\theta_{i,k}^{rel}) (\mathbf{R}_{\beta_k}^{\alpha_k})^T (\delta\theta_{\beta_1}^{\alpha_1} - \delta\theta_{\beta_k}^{\alpha_k}) \quad (\text{B.15})$$

or

$$\left. \frac{d\mathcal{J}_{i,k}^{rot}}{d\epsilon} \right|_{\epsilon=0} = \mathbf{T}(\mathcal{J}_{i,k}^{rot}) (\mathbf{R}_{\beta_k}^{\alpha_k})^T (\delta\theta_{\beta_1}^{\alpha_1} - \delta\theta_{\beta_k}^{\alpha_k}). \quad (\text{B.16})$$

Appendix B.3. Linearization of helical constraints

Now, we derive the linearization of helical constraint terms. The linearization of the translational helical constraint (30) is given by

$$\frac{d}{d\epsilon} \mathcal{H}_k^{trans} = \delta \mathbf{r}_{\beta_{k_r}}^{\alpha_{k_r}} - \mathbf{R}^M \delta \mathbf{r}_{\beta_k}^{\alpha_k} - \left(\int_0^L \delta \mathbf{R}^M(l) ds \right) \mathbf{v}_0^M - \left(\int_0^L \mathbf{R}^M(l) ds \right) \delta \mathbf{v}_0^M - \delta \mathbf{R}^M(L) \mathbf{r}_{\beta_k}^{\alpha_k}. \quad (\text{B.17})$$

Note that, in the above linearization, we have also included the derivative with respect to macroscopic strains - this won't be needed while linearizing the weak form for prescribed macroscopic strains. The closed form expressions for the terms $\int \mathbf{R}^M dl$, $\delta \mathbf{R}^M$ and $\int \delta \mathbf{R}^M dl$, wherein $\delta = \frac{\partial}{\partial \kappa_i^M}$, can be seen in the Appendix B of Kumar et al. (2016). Next, the linearization of rotational helical constraint (37) is obtained. First, we define the helical constraint in (37) as

$$\mathcal{H}_k^{rot} \equiv \boldsymbol{\theta}_k^{rel} = \mathbf{0}. \quad (\text{B.18})$$

where $\boldsymbol{\theta}_k^{rel}$ is in turn defined using the left multiplicative update of (36) in the form

$$(\mathbf{R}_{\beta_{k_r}}^{\alpha_{k_r}})^T \mathbf{R}^M \mathbf{R}_{\beta_k}^{\alpha_k} = e^{\boldsymbol{\Theta}_k^{rel}} (\hat{\mathbf{R}}_{\beta_{k_r}}^{\alpha_{k_r}})^T (\hat{\mathbf{R}}_{\beta_k}^{\alpha_k}) \quad (\text{B.19})$$

and using the right multiplicative update as

$$(\mathbf{R}_{\beta_{k_r}}^{\alpha_{k_r}})^T \mathbf{R}^M \mathbf{R}_{\beta_k}^{\alpha_k} = (\hat{\mathbf{R}}_{\beta_{k_r}}^{\alpha_{k_r}})^T (\hat{\mathbf{R}}_{\beta_k}^{\alpha_k}) e^{\boldsymbol{\Theta}_{0,k}^{rel}} \quad (\text{B.20})$$

such that

$$\boldsymbol{\theta}_k^{rel} = (\hat{\mathbf{R}}_{\beta_{k_r}}^{\alpha_{k_r}})^T (\hat{\mathbf{R}}_{\beta_k}^{\alpha_k}) \boldsymbol{\theta}_{0,k}^{rel}. \quad (\text{B.21})$$

The linearization of the helical constraint is then given by

$$\frac{d}{d\epsilon} \mathcal{H}_k^{rot} = \frac{d}{d\epsilon} \boldsymbol{\theta}_k^{rel}. \quad (\text{B.22})$$

In order to obtain the linearization above, we first linearize equation (B.20), take its *axial* on both the sides and then apply (A.5) to obtain

$$(\mathbf{R}_{\beta_{k_r}}^{\alpha_{k_r}})^T (\mathbf{R}_M \delta \boldsymbol{\theta}_{\beta_k}^{\alpha_k} - \delta \boldsymbol{\theta}_{\beta_{k_r}}^{\alpha_{k_r}}) + (\mathbf{R}_{\beta_{k_r}}^{\alpha_{k_r}})^T \text{axial}(\delta \mathbf{R}^M (\mathbf{R}^M)^T) = (\hat{\mathbf{R}}_{\beta_{k_r}}^{\alpha_{k_r}})^T \hat{\mathbf{R}}_{\beta_k}^{\alpha_k} \mathbf{T}^{-1} (\boldsymbol{\theta}_{0,k}^{rel}) \frac{d\boldsymbol{\theta}_{0,k}^{rel}}{d\epsilon}. \quad (\text{B.23})$$

Using (B.21) and (A.7), we finally obtain

$$\frac{d\boldsymbol{\theta}_k^{rel}}{d\epsilon} = \mathbf{T}(\boldsymbol{\theta}_k^{rel}) (\mathbf{R}_{\beta_{k_r}}^{\alpha_{k_r}})^T (\mathbf{R}^M \delta \boldsymbol{\theta}_{\beta_k}^{\alpha_k} - \delta \boldsymbol{\theta}_{\beta_{k_r}}^{\alpha_{k_r}}) + \mathbf{T}(\boldsymbol{\theta}_k^{rel}) (\mathbf{R}_{\beta_{k_r}}^{\alpha_{k_r}})^T \text{axial}(\delta \mathbf{R}^M (\mathbf{R}^M)^T) \quad (\text{B.24})$$

or

$$\frac{d\mathcal{H}_k^{rot}}{d\epsilon} = \mathbf{T}(\mathcal{H}_k^{rot}) (\mathbf{R}_{\beta_{k_r}}^{\alpha_{k_r}})^T (\mathbf{R}^M \delta \boldsymbol{\theta}_{\beta_k}^{\alpha_k} - \delta \boldsymbol{\theta}_{\beta_{k_r}}^{\alpha_{k_r}}) + \mathbf{T}(\mathcal{H}_k^{rot}) (\mathbf{R}_{\beta_{k_r}}^{\alpha_{k_r}})^T \text{axial}(\delta \mathbf{R}^M (\mathbf{R}^M)^T). \quad (\text{B.25})$$

Here again, the derivatives of macroscopic strain terms vanish if they are assumed constant.

Appendix C. Configuration of a nearly helical rod

The initial configuration of the nearly helical rod in [Chang et al. \(2022\)](#) can be written as $\mathbf{r} = X(\Phi)\mathbf{e}_1 + Y(\Phi)\mathbf{e}_2 + Z(\Phi)\mathbf{e}_3$ where

$$\begin{aligned}
X(\Phi) &= \begin{cases} r_h \sin^2 \left(\frac{\pi Z^2(\Phi)}{2p_j^2} \right) \sin \Phi, & 0 \leq \Phi < \frac{\pi}{2} \\ r_h \sin \Phi, & \frac{\pi}{2} \leq \Phi < (2N_h + \frac{1}{2}) \pi \\ r_h \sin^2 \left(\frac{\pi(N_h \rho_h + 2p_j - Z(\Phi))^2}{2p_j^2} \right) \sin \Phi, & (2N_h + \frac{1}{2}) \pi \leq \Phi \leq (2N_h + 1)\pi \end{cases} \\
Y(\Phi) &= \begin{cases} -r_h \sin^2 \left(\frac{\pi Z^2(\Phi)}{2p_j^2} \right) \cos \Phi, & 0 \leq \Phi < \frac{\pi}{2} \\ -r_h \cos \Phi, & \frac{\pi}{2} \leq \Phi < (2N_h + \frac{1}{2}) \pi \\ -r_h \sin^2 \left(\frac{\pi(N_h \rho_h + 2p_j - Z(\Phi))^2}{2p_j^2} \right) \cos \Phi, & (2N_h + \frac{1}{2}) \pi \leq \Phi \leq (2N_h + 1)\pi \end{cases} \\
Z(\Phi) &= \begin{cases} \frac{p_h}{4\pi^3} \left(3 - \frac{16p_j}{p_h} \right) \Phi^3 + \frac{p_h}{4\pi^2} \Phi^2 + \frac{p_h}{16\pi} \left(\frac{48p_j}{p_h} - 5 \right) \Phi, & 0 \leq \Phi < \frac{\pi}{2} \\ \frac{p_h}{2\pi} \left(\Phi - \frac{\pi}{2} \right) + p_j, & \frac{\pi}{2} \leq \Phi < (2N_h + \frac{1}{2}) \pi \\ N_h p_h + 2p_j - \frac{p_h}{4\pi^3} \left(3 - \frac{16p_j}{p_h} \right) [(2N_h + 1)\pi - \Phi]^3 \\ \quad - \frac{p_h}{4\pi^2} [(2N_h + 1)\pi - \Phi]^2 - \frac{p_h}{16\pi} \left(\frac{48p_j}{p_h} - 5 \right) [(2N_h + 1)\pi - \Phi], & (2N_h + \frac{1}{2}) \pi \leq \Phi \leq (2N_h + 1)\pi \end{cases}
\end{aligned}$$

Appendix D. Cross RVE analytical derivations

In this section, we derive the analytical formulas of macroscopic stiffnesses $\mathbb{C}_{22}^M, \mathbb{C}_{33}^M, \mathbb{C}_{44}^M$ given in Table 1. The assumptions in the derivations are (i) infinitesimal macroscopic strain and (ii) Euler-Bernouli beam model for microscale rods. Figure D.21 shows the three cases of uniform macroscopic in-plane shear (left figure), extension (middle figure) and in-plane bending (right figure). Note that we have centered the RVE at the origin in order to simplify the analysis. The rod OC is isolated from the cross RVE and the bending moment-deflection problem is solved for the three deformation cases. Firstly, bending moment balance at an arbitrary point x on the microscale rod OC is given by

$$-M_x + M + P(l - x) = 0. \quad (\text{D.1})$$

Here the sign convention in the local coordinate system of the beam is - upward deflection and counter-clockwise moment are considered positive. The quantities P and M are unknown reaction force and moment from the joint connections of the rod with the neighbouring image. Assuming small deformation of microscale rod OC , one can write

$$M_x = EI \frac{d^2 y}{dx^2} \quad (\text{D.2})$$

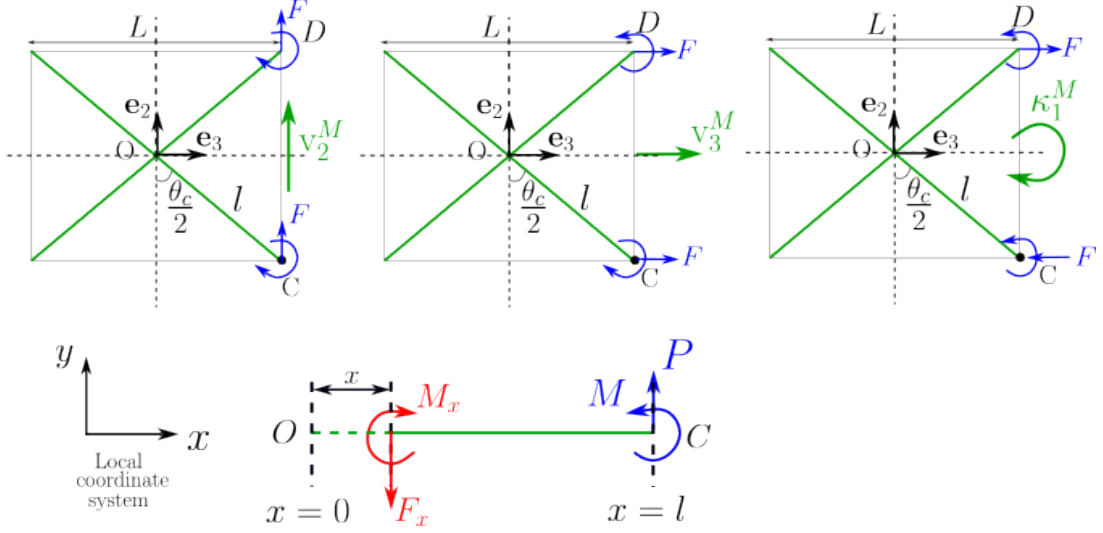


Figure D.21: Cross RVE schematic under uniform in plane shearing ($P = F \sin \frac{\theta_c}{2}$), stretching ($P = F \cos \frac{\theta_c}{2}$) and bending ($P = -F \cos \frac{\theta_c}{2}$).

where $y(x)$ is the transverse deflection. Substituting the above microscale moment-curvature relationship in (D.1) and integrating, we get the equations for slope and deflection as

$$\begin{aligned} EI \frac{dy}{dx} &= Mx + P\left(lx - \frac{x^2}{2}\right) + c_1 \quad \text{and} \\ EIy &= M\frac{x^2}{2} + P\left(l\frac{x^2}{2} - \frac{x^3}{6}\right) + c_1x + c_2, \end{aligned} \quad (\text{D.3})$$

respectively. Here c_1 and c_2 are arbitrary integration constants and are obtained for the specific cases of macroscopic strain considering appropriate boundary conditions. Now, let us consider each case of macroscopic strain separately.

Appendix D.1. Extensional stiffness

In case of uniform extension, the force P on the rod OC is given by

$$P = F \cos \frac{\theta_c}{2} \quad (\text{D.4})$$

and the boundary conditions are

$$y(0) = 0, \quad y'(0) = 0, \quad y'(l) = 0 \quad (\text{D.5})$$

in the local coordinate system. Using the force expression (D.4) and the boundary conditions (D.5), we get

$$\begin{aligned} EIy' &= F \cos \frac{\theta_c}{2} \left(lx - \frac{x^2}{2}\right) + Mx, \\ EIy &= F \cos \frac{\theta_c}{2} \left(l\frac{x^2}{2} - \frac{x^3}{6}\right) + 0.5Mx^2, \\ M &= -0.5Fl \cos \frac{\theta_c}{2}. \end{aligned} \quad (\text{D.6})$$

From the above equations, the transverse displacement at $x = l$ is given by

$$y(l) = \frac{Fl^3}{12EI} \cos \frac{\theta_c}{2}. \quad (\text{D.7})$$

The displacement of point C is then given by

$$\delta = y(l) \cos \frac{\theta_c}{2} = \frac{Fl^3}{12EI} \cos^2 \frac{\theta_c}{2}. \quad (\text{D.8})$$

Due to periodicity, the same displacement occurs at the left face of the RVE, resulting in the total deformation of the RVE to be 2δ . Thus, the total extensional strain of the RVE is given by

$$v_3^M = \frac{2\delta}{L} = \frac{\delta}{l \sin \frac{\theta_c}{2}} \frac{Fl^2}{12EI} \frac{\cos^2 \frac{\theta_c}{2}}{\sin \frac{\theta_c}{2}} \quad (\text{D.9})$$

and the total axial force on the right face of the RVE is

$$n_3^M = 2F. \quad (\text{D.10})$$

The net moment on the right face is zero which results in the equal and opposite reaction moments on points C and D . Finally, using (D.9) and (D.10), the extensional stiffness of the RVE is

$$\mathbb{C}_{33}^M = \frac{n_3^M}{v_3^M} = \frac{24EI \tan \frac{\theta_c}{2}}{l^2 \cos \frac{\theta_c}{2}}. \quad (\text{D.11})$$

The above linear relationship between n_3^M and v_3^M assumes small deformation at the macroscale.

Appendix D.2. In-plane bending stiffness

In case of uniform in-plane bending curvature, the force P on the rod OC is given by

$$P = -F \cos \frac{\theta_c}{2} \quad (\text{D.12})$$

and the boundary conditions are

$$y(0) = 0, \quad y'(0) = 0, \quad y'(l) = -\frac{k_1^M l}{2} \quad (\text{D.13})$$

in the local coordinate system. Using equations (D.3), (D.12), and (D.13), we get

$$\begin{aligned} EIy' &= -F \cos \frac{\theta_c}{2} \left(lx - \frac{x^2}{2} \right) + Mx, \\ EIy &= -F \cos \frac{\theta_c}{2} \left(l \frac{x^2}{2} - \frac{x^3}{6} \right) + 0.5Mx^2, \\ M &= \frac{Fl}{2} \cos \frac{\theta_c}{2} - EI k_1^M \sin \frac{\theta_c}{2}. \end{aligned} \quad (\text{D.14})$$

Another equation is needed that is obtained by computing the deflection of the point C through geometry. Considering the figure D.22 wherein the RVE undergoes small bending

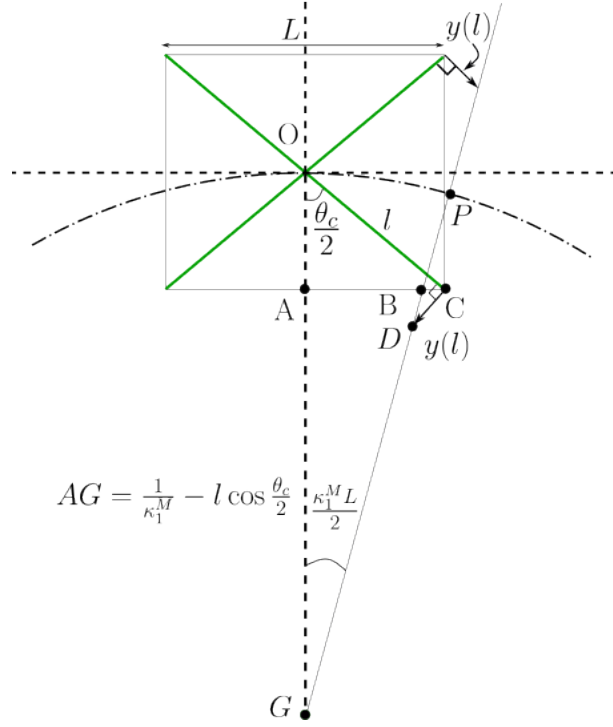


Figure D.22: A schematic of cross RVE undergoing small macroscale in-plane bending deformation (scaled here for clarity). The point G is at $\frac{1}{\kappa_1^M}$ distance from RVE origin O .

deformation (scaled for clarity) about the center G , we have

$$AG \left(\frac{k_1^M L}{2} \right) = AC - BC. \quad (\text{D.15})$$

And since BD is approximately perpendicular to BC in case of small deformation, we can say $BC = y(l) \cos \frac{\theta_c}{2}$. This results in

$$\begin{aligned} \left(\frac{1}{k_1^M} - l \cos \frac{\theta_c}{2} \right) \frac{k_1^M L}{2} &= \frac{L}{2} - y(l) \cos \frac{\theta_c}{2} \\ \Rightarrow y(l) &= k_1^M l^2 \sin \frac{\theta_c}{2}. \end{aligned} \quad (\text{D.16})$$

Substituting the above equation in (D.14)(b) with a negative sign because it is a downward deflection in the local coordinate system of the beam, we get

$$M = \frac{2Fl}{3} \cos \frac{\theta_c}{2} - 2EI k_1^M \sin \frac{\theta_c}{2}. \quad (\text{D.17})$$

Using (D.14)(c) and (D.17), we get

$$F = \frac{6EI k_1^M}{l} \tan \frac{\theta_c}{2}, \quad M = 2EI k_1^M \sin \frac{\theta_c}{2}. \quad (\text{D.18})$$

Now in the RVE coordinate system, the net moment about the axis passing through the center of the right face of the RVE into the paper is given by

$$M^{net} = m_1^M = 2Fl \cos \frac{\theta_c}{2} - 2M \quad (\text{D.19})$$

Finally, substituting (D.18) in (D.19), we get

$$m_1^M = 8EI k_1^M \sin \frac{\theta_c}{2}. \quad (\text{D.20})$$

Hence, the bending stiffness is

$$\mathbb{C}_{44}^M = \frac{m_1^M}{\kappa_1^M} = 8EI \sin \frac{\theta_c}{2}. \quad (\text{D.21})$$

Appendix D.3. In plane shear stiffness

In case of uniform in plane shear strain, the force P on the rod OC is given by

$$P = F \sin \frac{\theta_c}{2} \quad (\text{D.22})$$

and the boundary conditions on the rod OC are

$$y(0) = 0, \quad y(l) = v_2^M l \sin \frac{\theta_c}{2}, \quad y'(l) = 0. \quad (\text{D.23})$$

in the local coordinate system. Using (D.3), (D.22) and (D.23), we get

$$\begin{aligned} E I y' &= F \sin \frac{\theta_c}{2} \left(l x - \frac{x^2}{2} - \frac{l^2}{2} \right) + M(x - l), \\ E I y &= F \sin \frac{\theta_c}{2} \left(\frac{l x^2}{2} - \frac{x^3}{6} - \frac{l^2 x}{2} \right) + M(0.5x^2 - l x), \quad \text{and} \\ E I v_2^M l \sin \frac{\theta_c}{2} &= -\frac{F l^3}{6} \sin \frac{\theta_c}{2} - \frac{M l^2}{2} \end{aligned} \quad (\text{D.24})$$

Taking the moment balance about the \mathbf{e}_1 axis passing through the center of the RVE and equating it to be zero (since no external moment is applied on the junction), we get

$$\begin{aligned} 2Fl \sin \frac{\theta_c}{2} + 2M &= 0 \\ \Rightarrow M &= -Fl \sin \frac{\theta_c}{2} \end{aligned} \quad (\text{D.25})$$

Substituting the above equation in (D.24)(c), we get

$$\frac{F}{v_2^M} = \frac{3EI}{l^2} \frac{1}{\sin \frac{\theta_c}{2}}. \quad (\text{D.26})$$

The net macroscale force on the right face of the RVE is given by

$$\mathbf{n}_2^M = 2F. \quad (\text{D.27})$$

This results in the macroscopic shear stiffness as

$$\mathbb{C}_{22}^M = \frac{n_2^M}{v_2^M} = \frac{2F}{v_2^M} = \frac{6EI}{l^2} \frac{1}{\sin \frac{\theta_c}{2}}. \quad (\text{D.28})$$